Geosci. Model Dev., 14, 473–493, 2021
https://doi.org/10.5194/gmd-14-473-2021

Geoscientific Model Development
Open Access
EGU

Improving dust simulations in WRF-Chem v4.1.3 coupled with the GOCART aerosol module

Alexander Ukhov[1], **Ravan Ahmadov**[2,3], **Georg Grell**[3], **and Georgiy Stenchikov**[1]

[1]Division of Physical Sciences and Engineering, King Abdullah University of Science and Technology, Thuwal, Saudi Arabia
[2]CIRES, University of Colorado, Boulder, CO, USA
[3]NOAA Earth System Research Laboratory, Boulder, CO, USA

Correspondence: Alexander Ukhov (alexander.ukhov@kaust.edu.sa)

Received: 8 April 2020 – Discussion started: 19 May 2020
Revised: 6 December 2020 – Accepted: 11 December 2020 – Published: 25 January 2021

Abstract. In this paper, we rectify inconsistencies that emerge in the Weather Research and Forecasting model with chemistry (WRF-Chem) v3.2 code when using the Goddard Chemistry Aerosol Radiation and Transport (GOCART) aerosol module. These inconsistencies have been reported, and corrections have been implemented in WRF-Chem v4.1.3. Here, we use a WRF-Chem experimental setup configured over the Middle East (ME) to estimate the effects of these inconsistencies. Firstly, we show that the old version underestimates the $PM_{2.5}$ diagnostic output by 7 % and overestimates PM_{10} by 5 % in comparison with the corrected one. Secondly, we demonstrate that submicron dust particles' contribution was incorrectly accounted for in the calculation of optical properties. Therefore, aerosol optical depth (AOD) in the old version was 25 %–30 % less than in the corrected one. Thirdly, we show that the gravitational settling procedure, in comparison with the corrected version, caused higher dust column loadings by 4 %–6 %, PM_{10} surface concentrations by 2 %–4 %, and mass of the gravitationally settled dust by 5 %–10 %. The cumulative effect of the found inconsistencies led to the significantly higher dust content in the atmosphere in comparison with the corrected WRF-Chem version. Our results explain why in many WRF-Chem simulations PM_{10} concentrations were exaggerated. We present the methodology for calculating diagnostics we used to estimate the impacts of introduced code modifications. We share the developed Merra2BC interpolator, which allows processing Modern-Era Retrospective Analysis for Research and Applications, version 2 (MERRA-2) output for constructing initial and boundary conditions for chemical species and aerosols.

1 Introduction

Produced by wind erosion, mineral dust is one of the major drivers of climate over the Middle East (ME) (Osipov et al., 2015). Dust suspended in the atmosphere affects the energy budget by absorbing and scattering incoming solar radiation (Miller and Tegen, 1998) and by affecting cloud radiative properties (Forster et al., 2007). Dust can also negatively impact infrastructure and technology. For instance, reducing solar radiation reaching the Earth's surface dust decreases the output of photovoltaic systems. Moreover, dust deposition on solar panels deteriorates their efficiency (Sulaiman et al., 2014). Dust also has socioeconomic implications. Bangalath and Stenchikov (2015) showed that due to high dust loading, the tropical rain belt across the ME and north Africa strengthens and shifts northward, causing up to a 20 % increase in summer precipitation over the semi-arid strip south of the Sahara, including the Sahel. Frequent dust outbreaks have a profound effect on air quality in the ME region (Banks et al., 2017; Farahat, 2016; Alghamdi et al., 2015; Lihavainen et al., 2016). Air pollution is characterized by near-surface concentrations of particulate matter (PM), which comprise both $PM_{2.5}$ and PM_{10} (particles with diameters less than 2.5 and 10 µm, respectively). Dust is the major contributor to PM over the ME region (Ukhov et al., 2020a). The ME is also subjected to the inflow of dust from the nearby Sahara, which is another major dust source region (Osipov et al., 2015; Kalenderski and Stenchikov, 2016). Dust deposition fertilizes ocean surface waters and the seabed (Watson et al., 2000; Zhu et al., 1997).

Thus, given the impact of dust on climate, technology, human health, and ecosystems, an accurate description of dust

effects in numerical models is essential. In the first place, it requires careful description of the dust cycle: from emission at the Earth's surface, to transport in the atmosphere, and, finally, to removal by deposition.

Most of the studies mentioned above were conducted within the group of Atmospheric and Climate Modeling at King Abdullah University of Science and Technology (KAUST) using the Weather Research and Forecasting model with chemistry (WRF-Chem) (Skamarock et al., 2005; Grell et al., 2005; Powers et al., 2017). WRF-Chem is a popular open-source tool that is widely used to study atmospheric chemistry, air quality, and aerosols (Jish Prakash et al., 2015; Khan et al., 2015; Kalenderski et al., 2013; Kalenderski and Stenchikov, 2016; Parajuli et al., 2019; Anisimov et al., 2017; Osipov and Stenchikov, 2018). This model has been used extensively to study aerosols and their impact on air quality (Fast et al., 2006, 2009; Ukhov et al., 2020a, b; Parajuli et al., 2020), climate (Zhao et al., 2010, 2011; Chen et al., 2014; Fast et al., 2006) and to analyze dust outbreaks (Bian et al., 2011; Chen et al., 2014; Fountoukis et al., 2016; Ma et al., 2019; LeGrand et al., 2019; Su and Fung, 2015; Eltahan et al., 2018; Bukowski and van den Heever, 2020) in the ME and north Africa (Zhang et al., 2015; Flaounas et al., 2016; Rizza et al., 2017; Karagulian et al., 2019; Rizza et al., 2018), North America (Zhao et al., 2012), India (Dipu et al., 2013; Kumar et al., 2014), and Australia (Nguyen et al., 2019). Many aforementioned studies utilized the WRF-Chem model coupled with the Goddard Chemistry Aerosol Radiation and Transport (GOCART) aerosol module (Chin et al., 2002). The GOCART module simulates major tropospheric aerosol components, including sulfate, dust, black and organic carbon, and sea salt, and includes algorithms for dust and sea salt emissions, dry deposition, and gravitational settling. The GOCART module is one of the most popular aerosol modules used in WRF-Chem (Bian et al., 2011; Dipu et al., 2013; Kumar et al., 2014; Chen et al., 2014; Su and Fung, 2015; Zhang et al., 2015; Flaounas et al., 2016; Fountoukis et al., 2016; Rizza et al., 2017; Flaounas et al., 2017; Nabavi et al., 2017; Chen et al., 2018; Rizza et al., 2018; Ma et al., 2019; LeGrand et al., 2019; Parajuli et al., 2019; Yuan et al., 2019; Ukhov et al., 2020a; Eltahan et al., 2018; Nguyen et al., 2019; Bukowski and van den Heever, 2020).

However, working with the WRF-Chem/GOCART modeling system, we found a few inconsistencies in the physical parameterizations which affected its performance. Firstly, we found that the diagnostic output of $PM_{2.5}$ and PM_{10} was miscalculated. Secondly, the contribution of submicron dust particles was incorrectly accounted for in the Mie calculations of aerosol optical properties, and thus aerosol optical depth (AOD) was underestimated in comparison with observations. Thirdly, an inconsistency in the process of gravitational settling was leading to a violation of the dust and sea salt mass balance. The complete list of the WRF-Chem *chem_opt* namelist options that were affected is presented in Table 1.

All of these inconsistencies have affected WRF-Chem performance since 2 April 2010, when WRF-Chem v3.2 was released. We have reported all those issues, and they have been rectified in the WRF-Chem v4.1.3 code release. In this paper, we specifically discuss these corrections and evaluate how they have affected results. We demonstrate the methodology for calculating diagnostics that we used to estimate the impact of the introduced corrections. We also share with the community the Merra2BC interpolator (Ukhov and Stenchikov, 2020), which allows constructing initial and boundary conditions (IC&BC) for chemical species and aerosols using the Modern-Era Retrospective Analysis for Research and Applications, version 2 (MERRA-2) reanalysis (Randles et al., 2017). We believe that this discussion is in line with the open-source paradigm and will help users to better handle the code, understand physical links, and evaluate the sensitivity of the results to particular physical assumptions made in the code.

The paper is organized as follows: Sect. 2 describes the WRF-Chem model setup. In Sect. 3, a description of the inconsistencies found in the WRF-Chem code and their effects on the results is presented. Conclusions are presented in Sect. 4.

2 WRF-Chem experimental setup

To quantify the effects of introduced code modifications, we use our typical model setup which we previously adopted for simulating dust emissions using the WRF-Chem model coupled with the GOCART aerosol module. The WRF-Chem simulation domain (see Fig. 1) is centered at 28° N, 42° E, with a 10 km × 10 km horizontal grid (450 × 450 grid nodes). The vertical grid comprises 50 vertical levels with enhanced resolution closer to the ground. The model top boundary is set at 50 hPa. We use the *chem_opt*=300 namelist option, which corresponds to simulation using the GOCART aerosol module without ozone chemistry.

The unified Noah land surface model (*sf_surface_physics*=2) and the revised MM5 Monin–Obukhov scheme (*sf_sfclay_physics*=1) are chosen to represent land surface processes and surface layer physics. The Yonsei University scheme is chosen for planetary boundary layer (PBL) parameterization (*bl_pbl_physics*=1). The WRF single-moment microphysics scheme (*mp_physics*=4) is used for the treatment of cloud microphysics. The new Grell scheme (*cu_physics*=5) is used for cumulus parameterization. The Rapid Radiative Transfer Model (RRTMG) for both shortwave (*ra_sw_physics*=4) and longwave (*ra_lw_physics*=4) radiation is used for radiative transfer calculations. Only the aerosol direct radiative effect is accounted for. More details on the physical parameterizations used can be found at http://www2.mmm.ucar.edu/wrf/users/phys_references.html (last access: 20 January 2021).

Table 1. WRF-Chem *chem_opt* namelist options affected by the found inconsistencies.

chem_opt	Description	Found inconsistencies in calculation of		
		PM	Optical properties	Gravitational settling
2	MADE/SORGAM aerosols, RADM2 chemistry	−	−	+
11	Same as *chem_opt*=2 and some aqueous reactions	−	−	+
41	Same as *chem_opt*=2 and aqueous reactions	−	−	+
42	Same as *chem_opt*=41 using KPP library	−	−	+
109	MADE/VBS aerosols, RACM chemistry and aqueous reactions using KPP library	−	−	+
112	GOCART aerosols, MOZART chemistry using KPP library	+	+	+
300	GOCART aerosols, no ozone chemistry	+	+	+
301	GOCART aerosols, RACM chemistry using KPP library	+	+	+
303	GOCART aerosols, RADM2 chemistry	+	+	+
401	Dust concentration only	−	−	+

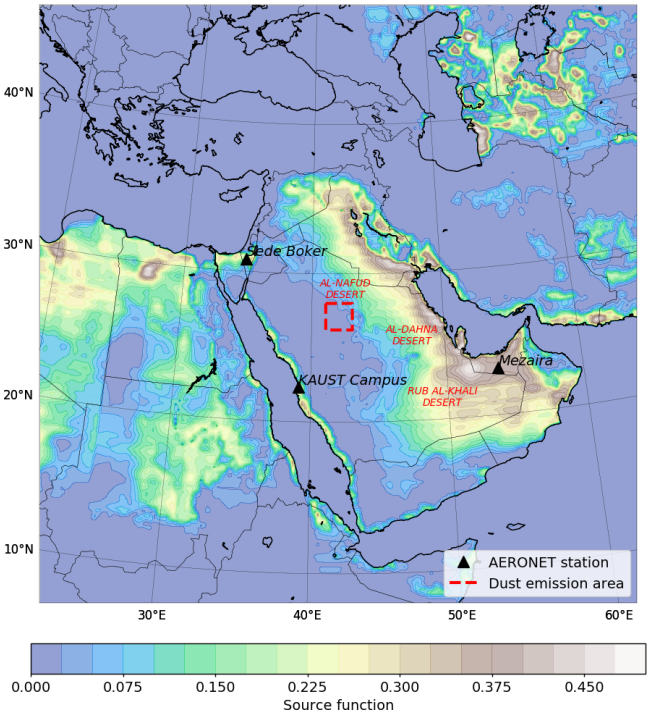

Figure 1. Simulation domain with marked locations of the AERONET sites. The red square corresponds to the dust emission area for conducting the dust mass balance check. Shaded contours correspond to source function S (Ginoux et al., 2001).

Dust size distribution in the GOCART module is approximated by five dust bins; see Table 2. Dust density is assumed to be 2500 kg m^{-3} for the first dust bin and 2650 kg m^{-3} for dust bins 2–5. In WRF-Chem, there are three dust emission schemes that can be used with GOCART: the original GOCART-WRF scheme (*dust_opt*=1) (Bagnold, 1941; Belly, 1964; Gillette and Passi, 1988), the Air Force Weather Agency (AFWA) scheme (*dust_opt*=3) (Marticorena and Bergametti, 1995; Su and Fung, 2015; Wang et al., 2015), and the University of Cologne (UoC) scheme (*dust_opt*=4) (Shao, 2001, 2004; Shao et al., 2011). The detailed description of all schemes is provided in LeGrand et al. (2019).

Table 2. Radii ranges (µm) of dust and sea salt bins used in the GOCART aerosol module.

	Bin				
	1	2	3	4	5
Dust	0.1–1.0	1.0–1.8	1.8–3.0	3.0–6.0	6.0–10.0
Sea salt	0.1–0.5	0.5–1.5	1.5–5.0	5.0–10.0	–

Here, we simulate dust emissions using the original GOCART-WRF scheme (*dust_opt*=1) proposed in Ginoux et al. (2001). Dust emission mass flux, F_p (µg m^{-2} s^{-1}) in each dust bin $p = 1, 2, \ldots, 5$ is defined by the relation

$$F_p = \begin{cases} C S s_p u_{10\,\mathrm{m}}^2 \left(u_{10\,\mathrm{m}} - u_\mathrm{t}\right), & \text{if } u_{10\,\mathrm{m}} > u_\mathrm{t} \\ 0, & \text{if } u_{10\,\mathrm{m}} \le u_\mathrm{t}, \end{cases} \quad (1)$$

where C (µg s^2 m^{-5}) is a spatially uniform factor which controls the magnitude of dust emission flux; S is the source function (Ginoux et al., 2001) (see Fig. 1) that characterizes the spatial distribution of dust emissions; $u_{10\,\mathrm{m}}$ is the horizontal wind speed at 10 m; u_t is the threshold velocity, which depends on particle size and surface wetness; s_p is a fraction of dust emission mass flux within dust bin p.

Sea salt size distribution in the GOCART module is approximated by four sea salt bins (see Table 2). Sea salt density is 2200 kg m^{-3}. Emission of sea salt is calculated according to Gong (2003).

2.1 Dust emission tuning

To adjust to regional conditions, dust emission in the model is calibrated to fit observed AOD and aerosol volume size distributions (AVSDs) obtained from the AErosol RObotic NETwork (AERONET; Holben et al., 1998). AERONET AOD observations represent the total AOD with contributions from all types of aerosols. But because in the ME dust is more prevalent than all other aerosols, we focus on dust emission only. More detailed information on dust emission tuning is provided in Ukhov et al. (2020a). For this study, we choose three AERONET sites (KAUST Campus, Mezaira, and Sede Boker) located within the domain (Fig. 1). We utilize level-2.0 (cloud-screened and quality-assured) AERONET AOD data. Note that from here onwards, we assume that AOD is given or calculated at 550 nm; see Appendix C.

2.1.1 Tuning the C parameter

To adjust dust emissions, we first tune the C factor from Eq. (1), as practiced in our own studies (Kalenderski et al., 2013; Jish Prakash et al., 2015; Khan et al., 2015; Kalenderski and Stenchikov, 2016; Anisimov et al., 2017; Parajuli et al., 2019, 2020; Ukhov et al., 2020a) and in the studies of other authors (Zhao et al., 2013; Kumar et al., 2014; Flaounas et al., 2017; Rizza et al., 2017). Our test runs indicate that for the ME, $C = 0.5$ achieves a good agreement between simulated and observed AOD at the KAUST Campus, Mezaira, and Sede Boker AERONET sites. Therefore, this sub-optimal value ($C = 0.5$) is retained in all subsequent runs.

2.1.2 Tuning the s_p fractions

We also tune s_p fractions from Eq. (1) to better reproduce the AVSDs provided by AERONET retrievals using the spectral deconvolution algorithm (SDA) (O'Neill et al., 2003). AERONET provides column-integrated AVSD $\mathrm{d}V/\mathrm{d}\ln r$ ($\mu\mathrm{m}^3\,\mu\mathrm{m}^{-2}$) on 22 logarithmically equidistant discrete points in the range of radii between 0.05 and 15 µm. For AVSDs, we use the AERONET v3, level-2.0 product (Dubovik and King, 2000).

In WRF-Chem, the default values of parameter s_p from Eq. (1) are {0.1, 0.25, 0.25, 0.25, 0.25}, for the DUST_1, DUST_2, …, DUST_5 dust bins, respectively. They control the size distribution of emitted dust. Our test runs indicate that when we use the default s_p values the dust volume size distributions in the atmosphere do not match those from AERONET. To achieve a better agreement between the modeled and AERONET volume size distributions, we adjust the fractions s_p to be {0.15, 0.1, 0.25, 0.4, 0.1}. The fractions s_p are set in the *phys/module_data_gocart_dust.F* file, array *frac_s*. We effectively increase the dust emission in the finest DUST_1 and in coarse DUST_4, and decrease those in DUST_2 and DUST_5. The size distribution of emitted dust is further processed in the atmosphere.

2.2 Initial and boundary conditions for meteorological parameters, chemical species, and aerosols

As is the case with any partial differential equation solver, WRF-Chem requires the IC&BC for meteorological parameters and chemical species. IC&BC for meteorological fields are derived from the ERA-Interim (Dee et al., 2011) global atmospheric reanalysis produced by the European Centre for Medium-Range Weather Forecasts (ECMWF). IC&BC values for chemical species are required to account for initial concentrations and inflow of aerosols and chemical species. The setting of improper lateral boundary conditions for aerosols and chemistry may significantly affect the result of the simulation. The role of lateral boundary conditions increases if the domain is located close to a significant source of dust or other chemicals. Concentrations of aerosols and chemicals within the domain are especially affected by the inflow through the lateral boundaries of species with long atmospheric lifetimes.

By default, WRF-Chem uses the idealized vertical profiles of a limited number of chemical species for calculating IC&BC. These profiles are obtained from the NOAA Aeronomy Lab Regional Oxidant Model (NALROM) model (Liu et al., 1996) simulation and are representative of the northern hemispheric midlatitude (North America) summer and clean environmental conditions. Another option in WRF-Chem is to use the output from the Model for Ozone And Related chemical Tracers, version 4 (MOZART-4) (Emmons et al., 2010), which is an offline tropospheric global chemical transport model.

The MERRA-2 reanalysis (Randles et al., 2017) provides a consistent distribution of aerosols and chemical species constrained by observations with the spatial resolution about 50 km. MERRA-2 aerosol and chemical fields are superior compared to those used previously in WRF-Chem. To calculate the chemical IC&BC using MERRA-2 output, we develop an interpolator (Merra2BC; Ukhov and Stenchikov, 2020), which uses gaseous and aerosol fields from MERRA-2 reanalysis to construct the IC&BC required by the WRF-Chem simulation. For more details regarding the Merra2BC interpolator, see Appendix A.

3 Results

In the discussion below, we refer to the WRF-Chem run with all inconsistencies fixed and with properly adjusted dust emission (see Sect. 2.1), with IC&BC constructed using the developed Merra2BC interpolator (see Sect. 2.2) as *ALL_OK*.

To quantify the effect of each inconsistency, we perform a WRF-Chem run where all the other corrections we discuss

Table 3. Default and updated values of the s_25, d_25, and d_10 mapping coefficients used to calculate $PM_{2.5}$ and PM_{10}.

	Default coefficients	Updated coefficients
s_25	0.942	$\ln(2.5/1)/\ln(3/1) = 0.834$
d_25	0.286	$\ln(2.5/2)/\ln(3.6/2) = 0.380$
d_10	0.870	$\ln(10/6)/\ln(12/6) = 0.737$

here are implemented, with the exception that we focus on a given time. The relative difference (%) of a specific set of variables in this run with respect to the *ALL_OK* run is presented as a measure of sensitivity to the chosen correction. All WRF-Chem runs are performed for 1–12 August 2016. At the end of this section, we estimate the cumulative effect of all inconsistencies. For this purpose, we performed WRF-Chem simulation over the period from 1 June to 31 December of 2016.

3.1 Calculation of $PM_{2.5}$ and PM_{10}

The subroutine *sum_pm_gocart* in *module_gocart_aerosols.F* calculates $PM_{2.5}$ and PM_{10} surface concentrations using the following formulas:

$$\begin{aligned} PM_{2.5} &= \rho \cdot (DUST_1 + DUST_2 \cdot d\_25 + SEAS_1 \\ &\quad + SEAS_2 \cdot s\_25), \\ PM_{10} &= \rho \cdot (DUST_1 + DUST_2 + DUST_3 \\ &\quad + DUST_4 \cdot d\_10 + SEAS_1 + SEAS_2 + SEAS_3), \end{aligned} \quad (2)$$

where ρ is the dry air density ($kg\,m^{-3}$), $DUST_{1,2,3,4}$ and $SEAS_{1,2,3}$ are the mixing ratios ($\mu g\,kg^{-1}$) of the dust in the first four bins and sea salt in the first three bins, respectively. The contribution of the dust and sea salt bins to $PM_{2.5}$ and PM_{10} is defined by the mapping coefficients d_25, d_10 for dust and s_25 for sea salt; see Eq. (2). Black and organic carbon and sulfate also contribute to PM, but over the ME region their contributions are small in comparison to dust and sea salt, and we omit them for the sake of brevity.

We suspect that the default mapping coefficients are calculated incorrectly. Therefore, we recalculated them assuming that dust and sea salt volume size distributions are functions of natural logarithm of particle radius. For example, interpolation in the logarithm space is more accurate than in the radius space, as aerosol size distributions are smoother functions of logarithm than radius. The updated values of mapping coefficients s_25, d_25, and d_10 along with their default values are presented in Table 3. Effectively, the contributions in $PM_{2.5}$ of sea salt $SEAS_2$ decreases, while that of dust $DUST_2$ increases. The contribution of $DUST_2$ in PM_{10} decreases.

The effects of using the updated mapping coefficients in place of default ones in PM calculation are shown in Fig. 2. We calculate the $PM_{2.5}$ and PM_{10} concentrations in the lowest model layer using Eq. (2). Surface concentrations of dust and sea salt are computed using the procedure presented in Appendix E. With the default mapping coefficients, the model on average yields 7 % lower $PM_{2.5}$ and 5 % higher PM_{10} concentrations over the ME.

3.2 Calculation of aerosol optical properties

For modeling in the ME, the treatment of optically active dust within the model is vitally important. AOD is calculated based on aerosol number density and aerosol optical properties, which depend on the aerosol size and refractive index. In WRF-Chem, a parameterized Mie theory (Ghan and Zaveri, 2007) is employed to calculate the aerosol optical properties. This parameterization is modified for the sectional representation of the aerosol size distribution by Fast et al. (2006) and Barnard et al. (2010), so the Mie subroutine requires input of dust number density or concentration in eight size intervals: {0.039–0.078, 0.078–0.156, 0.156–0.312, 0.312–0.625, 0.625–1.25, 1.25–2.5, 2.5–5.0, and 5.0–10.0} µm. These size intervals are identical to those used in the Model for Simulating Aerosol Interactions and Chemistry (MOSAIC) microphysical module (Zaveri et al., 2008). Therefore, we further refer to them as MOSAIC bins ($MOS_{1,2,3,4,5,6,7,8}$).

To correctly calculate the dust optical properties, we implement two corrections in the subroutine *optical_prep_gocart()* in *module_optical_averaging.F* that compute the volume-averaged refractive index needed for Mie calculations.

3.2.1 Effect of small particles

In WRF-Chem's GOCART aerosol module, dust particle sizes span 2 orders of magnitude, from 0.1 to 10 µm; see Table 2. However, we find that dust particles with radii between 0.1 and 0.46 µm are incorrectly accounted for in the Mie calculations of aerosol optical properties. Their mixing ratio is mapped on coarser MOSAIC bins than is required. Since finer particles have a stronger effect on AOD per unit mass in comparison to coarser particles, the model AOD decreases. As a result, when tuning dust emission, we push the model to emit more dust into the atmosphere, in order to fit the observed AOD. We rectify this error by correcting mapping fractions of $DUST_1$ into MOSAIC bins; see Table 4.

Table 4 presents the mapping fractions of the GOCART dust bins ($DUST_{1,2,3,4}$) to the MOSAIC bins ($MOS_{1,2,3,4,5,6,7,8}$) before and after correction. We do not include GOCART dust bin $DUST_5$ in Table 4 since it is out of the MOSAIC size range and is therefore not accounted for in the mass redistribution. Also, the mass from $DUST_4$ is only partially accounted for. After the changes, the dust mass from the $DUST_1$ bin is redistributed between finer $MOS_{3,4,5,6}$ bins compared to the original WRF-Chem where the entire $DUST_1$ mixing ratio was mapped on the coarser $MOS_{5,6}$ bins.

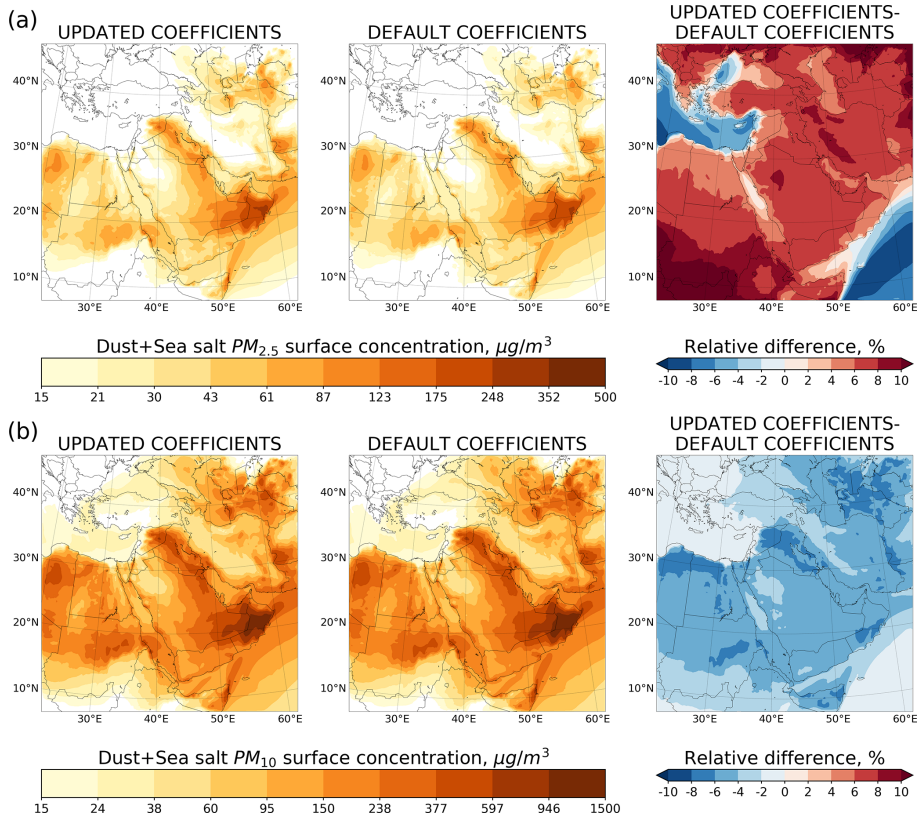

Figure 2. Average dust and sea salt $PM_{2.5}$ **(a)** and PM_{10} **(b)** surface concentration ($\mu g\ m^{-3}$) calculated using default and updated coefficient values and relative difference (%).

Table 4. Dust mass redistribution between GOCART and MOSAIC bins before and after inclusion of dust particles with radii $\geq 0.1\,\mu m$ into calculation of aerosol optical properties.

Before inclusion	MOS_1	MOS_2	MOS_3	MOS_4	MOS_5	MOS_6	MOS_7	MOS_8
$DUST_1$	0.0	0.0	0.0	0.0	0.305	0.695	0.0	0.0
$DUST_2$	0.0	0.0	0.0	0.0	0.0	0.312	0.688	0.0
$DUST_3$	0.0	0.0	0.0	0.0	0.0	0.0	0.583	0.417
$DUST_4$	0.0	0.0	0.0	0.0	0.0	0.0	0.0	0.666
After inclusion								
$DUST_1$	0.0	0.0	0.062	0.174	0.347	0.417	0.0	0.0
$DUST_2$	0.0	0.0	0.0	0.0	0.0	0.312	0.688	0.0
$DUST_3$	0.0	0.0	0.0	0.0	0.0	0.0	0.583	0.417
$DUST_4$	0.0	0.0	0.0	0.0	0.0	0.0	0.0	0.666

3.2.2 Bin concentration interpolation

Originally, the subroutine *optical_prep_gocart()* redistributes dust and sea salt mass from GOCART into MOSAIC bins, using the assumption that dust size distribution is a function of particle radius. Consistent with Sect. 3.1, here we conduct interpolation assuming that dust distribution is a function of natural logarithm of radius. This modification causes changes in the mass redistribution between the GOCART and MOSAIC bins (see Table 5) and increases the contribution of small dust particles into the AOD. Because the dust size distribution is a smoother function of the logarithm of a radius than the radius itself, interpolation is more accurate in logarithms than in radii.

To estimate the effect of these two corrections, we develop the WRF-Chem simulation *NON_LOG_046*, where only these two inconsistencies are not fixed, and compare the resulting AOD with that from the *ALL_OK* run. The AOD val-

Table 5. Dust mass redistribution between GOCART and MOSAIC bins based on the assumption that bin concentration is a function of radius and on the assumption that bin concentration is a function of natural logarithm radius.

Function of radius	MOS_1	MOS_2	MOS_3	MOS_4	MOS_5	MOS_6	MOS_7	MOS_8
$DUST_1$	0.0	0.0	0.062	0.174	0.347	0.417	0.0	0.0
$DUST_2$	0.0	0.0	0.0	0.0	0.0	0.312	0.688	0.0
$DUST_3$	0.0	0.0	0.0	0.0	0.0	0.0	0.583	0.417
$DUST_4$	0.0	0.0	0.0	0.0	0.0	0.0	0.0	0.666
Function of natural logarithm radius								
$DUST_1$	0.0	0.0	0.194	0.301	0.301	0.204	0.0	0.0
$DUST_2$	0.0	0.0	0.0	0.0	0.0	0.380	0.620	0.0
$DUST_3$	0.0	0.0	0.0	0.0	0.0	0.0	0.643	0.357
$DUST_4$	0.0	0.0	0.0	0.0	0.0	0.0	0.0	0.737

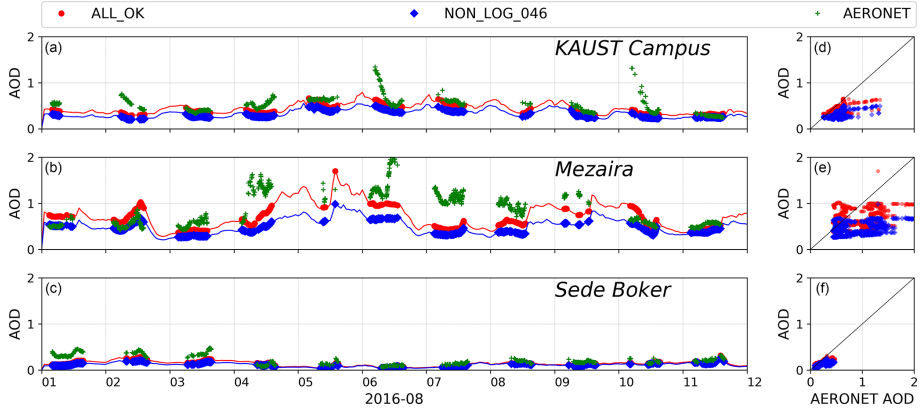

Figure 3. AOD time series **(a–c)** and scatter plots **(d–f)** from *NON_LOG_046* and *ALL_OK* runs (blue and red lines) and AERONET AOD (green markers) at KAUST Campus, Mezaira, and Sede Boker. WRF-Chem's AOD is interpolated to the times (blue diamonds and red dots) when AERONET AOD measurements were conducted.

ues are computed as described in Appendix C. As expected, the AOD increases after the corrections. Figure 3 compares the AOD obtained from the *ALL_OK* and *NON_LOG_046* runs with AERONET AOD at KAUST Campus, Mezaira, and Sede Boker. Because AERONET conducts measurements during daylight hours only, we interpolate WRF-Chem AOD to the AERONET measurement times.

To quantify the capability of WRF-Chem in reproducing the AERONET AOD, we calculate the Pearson correlation coefficient R and mean bias (see Appendix B) of simulated AOD with respect to the AERONET AOD observations for the entire simulation period (see Table 6). The corrections improve the correlation for Mezaira and Sede Boker and cause a 2-fold reduction in the mean bias in KAUST Campus and Mezaira. The magnitude and temporal evolution of the AOD time series is well correlated in both runs (with and without corrections) with the observed AERONET AOD at all sites only when the AERONET AOD < 1. For dusty conditions with AOD > 1, WRF-Chem with the original GOCART scheme (*dust_opt*=1) struggles to capture the observations. We find the worst correlation ($R = 0.42$) and highest mean bias (-0.19) with AERONET AOD at the Mezaira station, which is located in a major dust source region (see Fig. 1). We obtain higher correlations with AERONET AOD of 0.66 and 0.75 for the KAUST Campus and Sede Boker stations, respectively. Both of these stations are located outside the main dust source regions.

Table 6. Pearson correlation coefficient R and mean bias calculated for AOD time series from two runs with respect to AERONET AOD observations.

	KAUST Campus		Mezaira		Sede Boker	
	R	Bias	R	Bias	R	Bias
ALL_OK	0.66	−0.10	0.42	−0.19	0.75	−0.07
NON_LOG_046	0.66	−0.20	0.36	−0.38	0.67	−0.11

Figure 4 shows the averaged AOD fields obtained from the *ALL_OK* and *NON_LOG_046* runs, as well as their relative difference (%). We conclude that due to these two inconsistencies, averaged AOD obtained from the *NON_LOG_046*

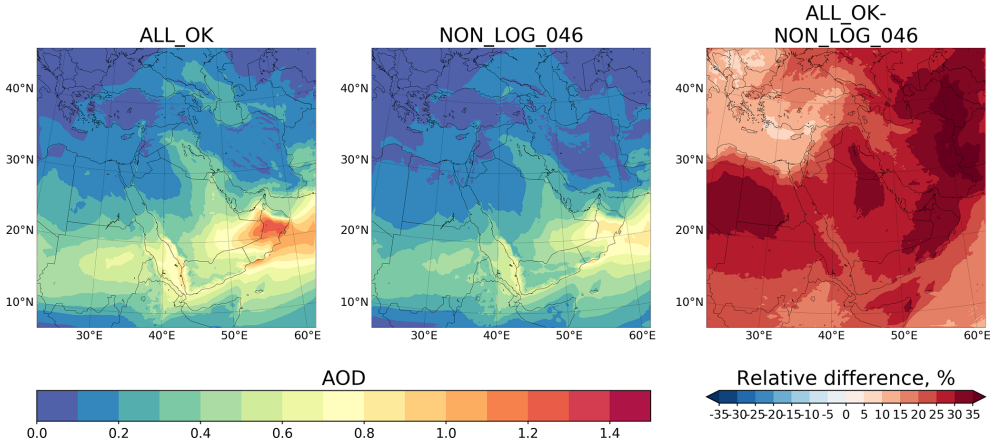

Figure 4. Averaged AOD fields obtained from the *ALL_OK* and *NON_LOG_046* runs and their relative difference (%).

run is lower by 25 %–30 % on average over the ME in comparison with the *ALL_OK* run. Over Libya, Egypt, Oman, Iran, Azerbaijan, Turkmenistan, and Pakistan, the difference is even higher, reaching 30 %–35 %.

3.3 Gravitational settling

We find that in the original WRF-Chem code the gravitational settling of dust and sea salt is calculated incorrectly. The default finite-difference scheme (implemented in the subroutine *settling()* file *module_gocart_settling.F*) does not account for change in air density when it calculates deposition mass flux. Thus, in the course of the gravitational settling, the total mass of dust and sea salt in the atmosphere increases, violating their mass balances. We introduce the new finite-difference scheme, which allows conservation of the mass of dust and sea salt in the course of gravitational settling in the atmosphere. The new finite-difference scheme is provided below.

The change of aerosol mixing ratio due to gravitational settling at downward directed velocity w is given by the following differential equation:

$$\frac{\partial(\rho q)}{\partial t} = \frac{\partial(\rho q w)}{\partial z}, \tag{3}$$

where q is the aerosol mass mixing ratio ($\mu g\,kg^{-1}$) and ρ is the dry air density ($kg\,m^{-3}$). Using the first-order upwind scheme, this equation can be discretized into the following form:

$$\frac{q_k^{n+1}\rho_k^{n+1} - q_k^n\rho_k^n}{\Delta t} = \frac{q_{k+1}^n\rho_{k+1}^{n+1}w_{k+1}^n - q_k^n\rho_k^{n+1}w_k^n}{\Delta z_k}, \tag{4}$$

where Δz_k is the depth of the k model level, and Δt is the model time step. Subscript k denotes the model levels and superscript n is the time level. Taking into account that the calculation of gravitational settling is split from the calculation of the continuity equation, we assume $\rho_k^{n+1} \approx \rho_k^n$ and get the following solution:

$$q_k^{n+1} = q_k^n\left(1 - \frac{\Delta t w_k^n}{\Delta z_k}\right) + q_{k+1}^n\frac{\Delta t w_{k+1}^n}{\Delta z_k}\frac{\rho_{k+1}^{n+1}}{\rho_k^{n+1}}. \tag{5}$$

Equation (5) is solved for each model column from the top to the bottom.

To validate the modified finite-difference scheme, we zero dust emissions across the whole domain, except for the 200 km × 200 km area located at the center of the domain; see Fig. 1. Only the first 10 simulation hours of dust emissions within this area are included. We prohibit the inflow of dust from the domain boundaries by zeroing the corresponding boundary conditions, and we zero the initial dust concentrations to simplify calculation of the dust mass balance, which we compute using the following balance relation:

$$\text{Dust in the atmosphere} = \text{Emitted dust} - (\text{Grav. settled dust} + \text{Dry deposited dust}). \tag{6}$$

The amount of dust in the atmosphere is controlled by dust emission and dust deposition. The latter comprises gravitational settling and dry deposition. For the sake of clarity, we refrain from introducing other dust removal processes, such as subgrid wet deposition (*conv_tr_wetscav*=0). The procedure of calculation of these diagnostics using the WRF-Chem output is provided in Appendix F.

Figure 5 demonstrates the evolution of the components of the dust mass balance (see Eq. 6) from the two runs, with and without correction of the gravitational settling procedure. For the analysis, we took only the first 40 h of output because, after that time the dust plume reaches the lateral boundaries of the domain. As shown in Fig. 5a, the dashed red line corresponding to the sum of deposited mass and dust mass in the atmosphere diverges from the dash-dotted purple line, which corresponds to the mass of emitted dust. This difference reaches 2.16 % before the dust plume reaches the boundaries of the domain. The run using the original gravitational settling gains the dust mass represented by the blue

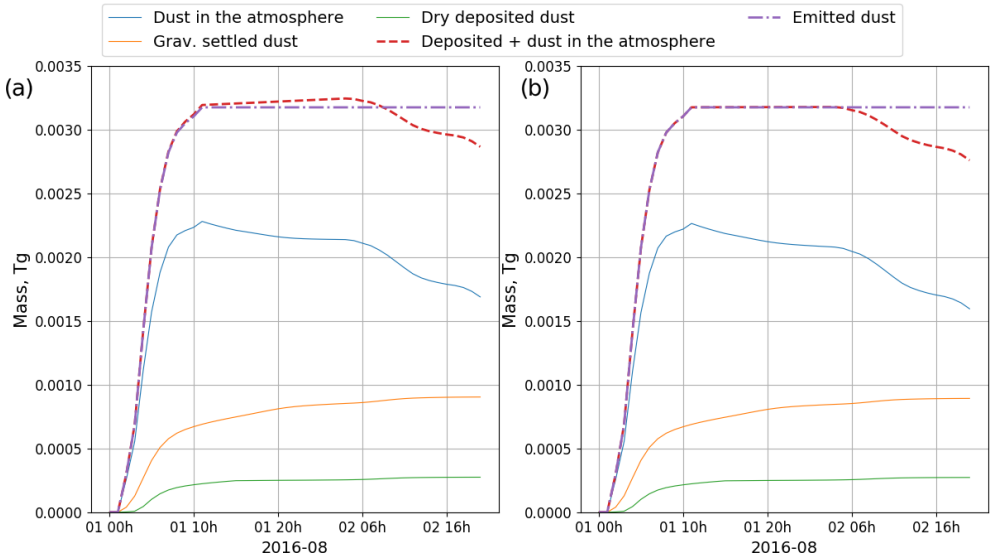

Figure 5. Dust mass balance check **(a)** before and **(b)** after correction of gravitational settling. Deposited dust is the combination of gravitationally settled dust and dry deposited dust.

line, due to the error in calculating gravitational settling, as discussed above. This is in contrast with Fig. 5b, where we see perfect agreement between the amounts of deposited dust plus dust in the atmosphere and emitted dust until the dust plume reaches the boundaries of the domain. Thus, this inconsistency in the gravitational settling subroutine is significant, as the error of 2.16 % of total emitted mass accumulates within $\approx$ 20 h. For a larger domain, this imbalance will be more significant. This effect is especially important in the low-latitude desert regions. Zhang et al. (2015), Dipu et al. (2013), and Huang et al. (2010) reported that in dry subtropics the boundary layer height can reach 6–7 km, which promotes the transport of dust particles to this altitude. When dust particles are settling from higher altitudes, a larger mass imbalance is accumulated.

We estimate the effect of the gravitational settling error by comparing averaged total dust column loadings (see Fig. 6a), accumulated gravitationally settled dust (see Fig. 6b), and averaged dust and sea salt PM_{10} surface concentrations (see Fig. 6c) obtained in the *ALL_OK* and *NOT_FIXED_GRAV_SETTLING* runs, where the latter corresponds to the run with error in gravitational settling. We perform a comparison in terms of relative differences (%) in the runs, with and without corrections. Dust column loadings, gravitationally settled dust, and PM_{10} surface concentrations are calculated according to the methodology described in Appendix Sects. D, F3, and E, respectively. According to Fig. 6a–c, we observe higher negative values of relative difference over non-dust-source regions (see Fig. 1), i.e., over Sudan, Turkey, Yemen, Eritrea, Djibouti, and Ethiopia. In contrast, the relative differences over dust source regions, which include Egypt and the eastern part of Arabian Peninsula, are close to zero. Coarse dust particles have shorter lifetimes in the atmosphere because of their higher deposition velocities. Thus, coarse dust particles are mostly deposited in the dust source regions, which explains close to zero values of relative difference in this region. Fine dust particles have longer atmospheric lifetime and thus can be transported over longer distances. The discrepancies in the descriptions of the life cycle of fine dust explain larger relative errors in non-dust regions, as mentioned above.

Thus, we can conclude that in the *NOT_FIXED_GRAV_SETTLING* run, the total dust column loading is higher by 4 %–6 % over the ME in comparison with the *ALL_OK* run. The computed total amount of dust in the atmosphere (see Appendix F4) was 6.41 and 6.72 Tg for the *ALL_OK* and *NOT_FIXED_GRAV_SETTLING* runs, respectively. Hence, the amount of dust in the atmosphere is around 4.8 % higher. The total amount of gravitationally settled dust is 5 %–10 % higher on average in *NOT_FIXED_GRAV_SETTLING* run. The biggest difference (15 %–25 %) is observed in Sudan, Yemen, Eritrea, Djibouti, Ethiopia, and Turkey. The computed total amount of gravitationally settled dust (see Appendix F3) was 11 and 11.55 Tg for *ALL_OK* and *NOT_FIXED_GRAV_SETTLING* runs, respectively. Hence, the amount of gravitationally settled dust is around 5 % higher in the *NOT_FIXED_GRAV_SETTLING* run. Dust and sea salt PM_{10} surface concentrations (see Eq. 2 and Appendix E) are higher by 2 %–4 % on average over the ME in comparison with the *ALL_OK* run. We observe even bigger differences (6 %–10 %) over Eritrea, Djibouti, Ethiopia, and Turkey.

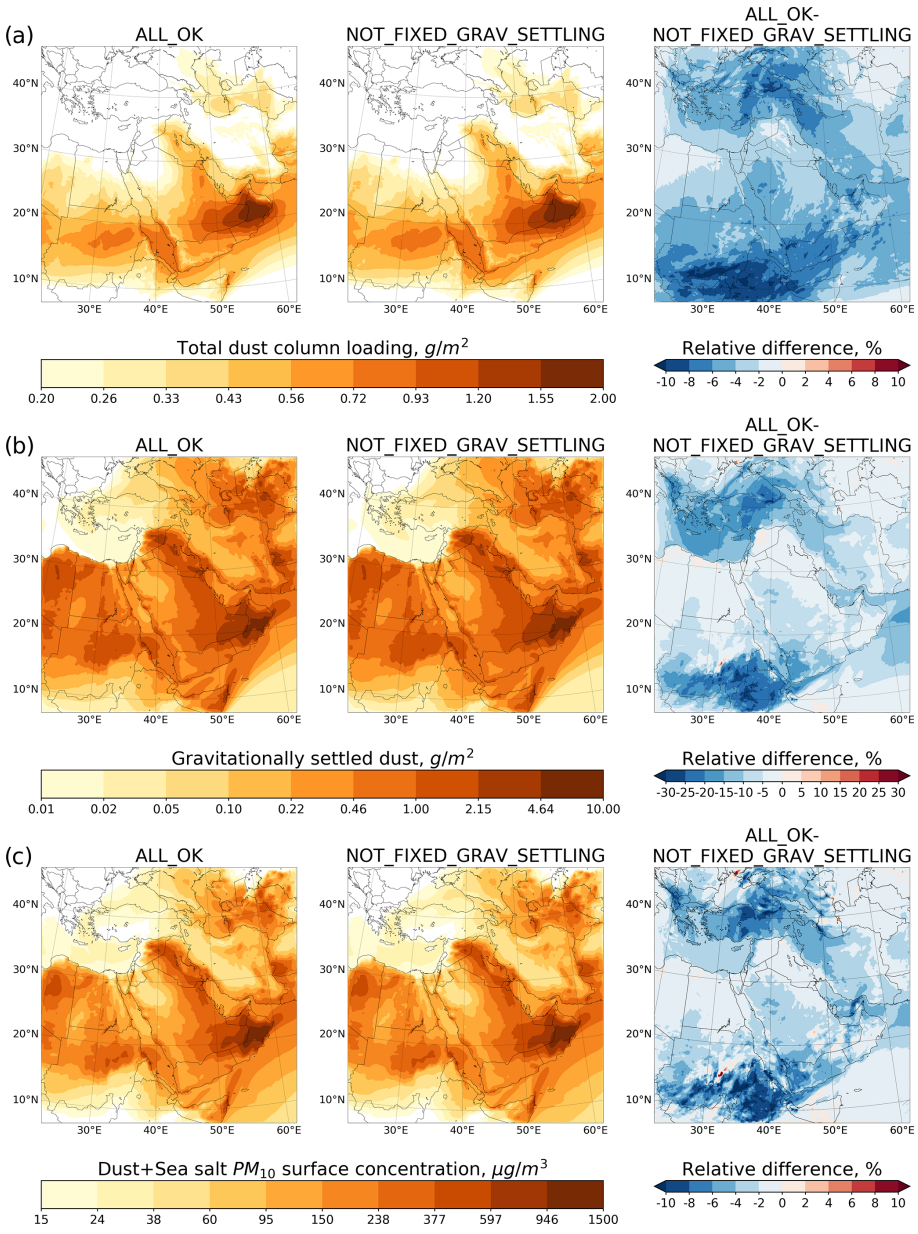

Figure 6. Comparison of *ALL_OK* and *NOT_FIXED_GRAV_SETTLING* runs. **(a)** Averaged total dust column loadings ($g\,m^{-2}$) and relative difference (%). **(b)** Gravitationally settled dust ($g\,m^{-2}$) and relative difference (%). **(c)** Averaged dust and sea salt PM_{10} surface concentrations ($\mu g\,m^{-3}$) and relative difference (%).

3.4 Case study

In the previous sections, we separately quantified the effect of each inconsistency in the WRF-Chem code and explained the associated physical links using short-term runs. In this section, we conduct a 7-month case study to demonstrate the cumulative effect of all inconsistencies. We ran two WRF-Chem simulations from 1 June to 31 December 2016, using the experimental setup described in Sect. 2. We refer to the WRF-Chem run, where all inconsistencies are intact, as *ALL_OLD*. We compare it with *ALL_OK* run in which all inconsistencies are corrected. The simulation period is chosen to take advantage of PM_{10} surface concentrations measurements conducted by the Saudi Authority for Industrial Cities and Technology Zones (MODON) in Riyadh, Jeddah, and Dammam (megacities of Saudi Arabia). More details on these measurements are provided in Ukhov et al. (2020a).

To adjust dust emissions in *ALL_OLD* run, we tuned the C factor from Eq. (1). Our test runs indicated that $C = 0.8$ provides the best agreement between simulated and observed AOD. For the *ALL_OK* run, we used $C = 0.5$ as before. Comparison of daily averaged AOD time series obtained

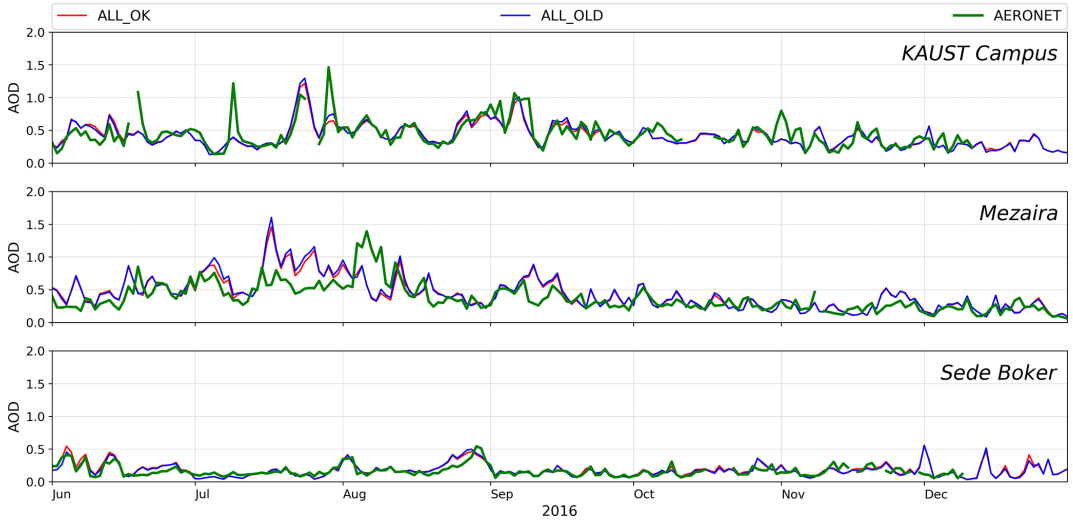

Figure 7. Daily averaged AOD time series from the *ALL_OK* and *ALL_OLD* runs (red and blue lines) and AERONET AOD (green line) at KAUST Campus, Mezaira, and Sede Boker.

from the *ALL_OK* and *ALL_OLD* runs with the AERONET AODs at KAUST Campus, Mezaira, and Sede Boker is presented in Fig. 7. AODs from both experiments are in good agreement with the AERONET AOD. The Pearson correlation coefficients and mean biases (see Appendix B) with respect to AERONET AOD are in the ranges of 0.62–0.75 and −0.03–0.07, respectively, for all AERONET sites. Thus, in the *ALL_OLD* run, the incorrect mapping of dust particles with radii between 0.1 and 0.46 µm causes stronger dust emissions in comparison with *ALL_OK* run.

The stronger dust emissions lead to increased dust surface concentrations and increased dust content in the atmosphere. Figure 8 shows comparison of the daily averaged PM_{10} surface concentrations obtained from the *ALL_OK* and *ALL_OLD* runs and from MODON observations in Riyadh, Jeddah, and Dammam. Modeled PM_{10} concentrations were computed using Eq. (2). PM_{10} constituents were sampled at the exact MODON stations locations. We used "default" and "updated" mapping coefficients (s_25, d_25, and d_10; see Table 3) for the evaluation of PM_{10} concentrations from the *ALL_OLD* and *ALL_OK* runs, respectively. Average MODON PM_{10} concentrations are 136, 206, and 229 ($\mu g\,m^{-3}$) for Jeddah, Riyadh, and Dammam, respectively. PM_{10} concentration time series from the *ALL_OK* run demonstrate better agreement with the MODON observations in comparison with the PM_{10} time series from the *ALL_OLD* run. In particular, mean biases with respect to MODON observations for *ALL_OK* and *ALL_OLD* runs are 2, 23, and 77, and 72, 182, and 275 ($\mu g\,m^{-3}$) for Jeddah, Riyadh, and Dammam, respectively; see Fig. 8. Thus, the PM_{10} concentration bias in *ALL_OK* is lower by 50 %–85 % in comparison with the *ALL_OLD* run.

Figure 9 demonstrates the averaged over the summer (June, July, August) of 2016 total dust column loadings ($g\,m^{-2}$) and their relative differences (%) obtained from the *ALL_OK* and *ALL_OLD* runs. In some locations, dust content in the atmosphere from the *ALL_OLD* run is higher by 80 % in comparison with the *ALL_OK* run. The total mass of dust in the atmosphere in the *ALL_OK* run yields 6.68 Tg in comparison with 10.92 Tg in the *ALL_OLD* run, so the difference exceeds 60 %.

3.5 Effect of initial and boundary conditions

We specifically conduct a sensitivity simulation to examine the impact of boundary conditions on PM_{10} surface concentration over the ME. In this simulation, boundary conditions are constructed using the developed Merra2BC interpolator (Ukhov and Stenchikov, 2020) (see Appendix A), and we zero the initial concentrations of dust and sea salt. The emissions of dust and sea salt within the domain are turned off (*dust_opt*=0, *seas_opt*=0). In this instance, PM_{10} concentrations are entirely determined by the inflow from the lateral boundaries. The averaged PM_{10} surface concentrations are presented in Fig. 10. PM_{10} concentrations are calculated using Eq. (2). Figure 10 shows the inflow of PM_{10} from Africa, central Asia, and the Indian Ocean. Dust is the major contributor to the PM_{10} transported from Africa and central Asia, whereas sea salt contributes to PM_{10} transported over the Indian Ocean.

4 Conclusions

In this paper, we discuss the inconsistencies found in the WRF-Chem v3.2 model coupled with the GOCART aerosol module. All of these inconsistencies are rectified in the WRF-Chem v4.1.3 code release. Here, we demonstrate the effect of the code rectification on WRF-Chem model performance.

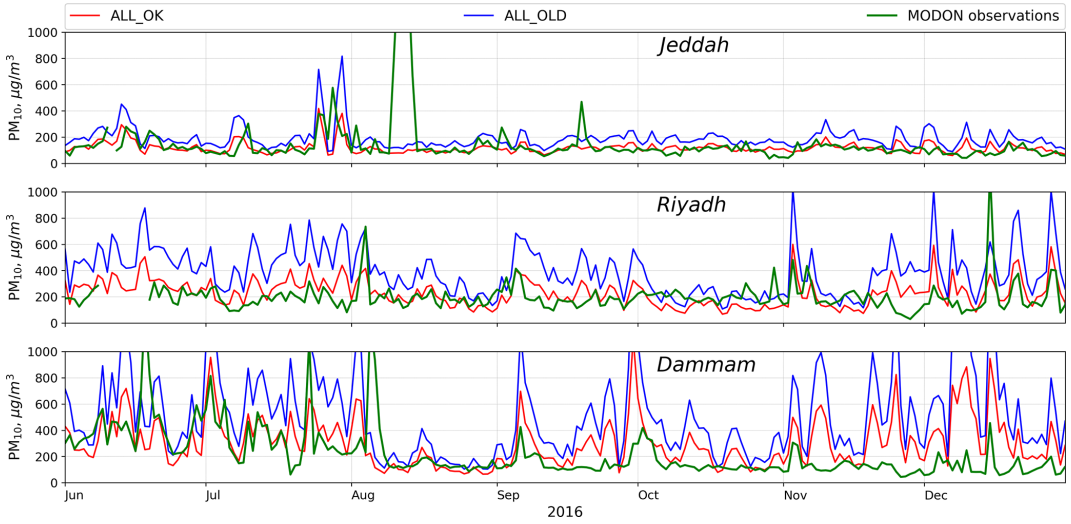

Figure 8. Daily averaged PM_{10} surface concentrations ($\mu g\,m^{-3}$) from the *ALL_OK* and *ALL_OLD* runs (red and blue lines) and from MODON observations (green line) at Jeddah, Riyadh, and Dammam.

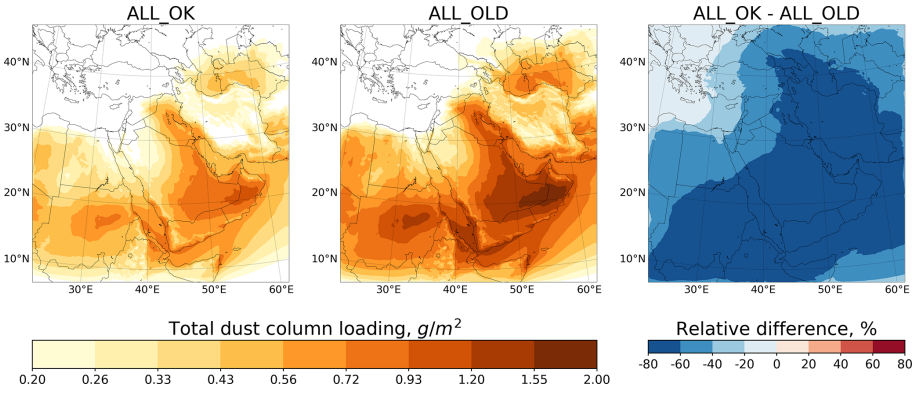

Figure 9. Averaged over the summer (June, July, August) of 2016 total dust column loadings ($g\,m^{-2}$) from the *ALL_OK* and *ALL_OLD* runs and relative difference (%).

We also demonstrate the methodology we employ to calculate diagnostics, which we then use to estimate the effects of the changes made. To make these assessments, we configure the WRF-Chem domain over the ME and run it with 10 km grid resolution. The runs discussed in this paper were performed over the period of 1–12 August 2016. The effect of each inconsistency was estimated using specifically designed WRF-Chem runs where only one model inconsistency was activated.

We found that in WRF-Chem v3.2 coupled with GOCART, the inconsistency in diagnostics of PM surface concentration caused a 7 % decrease in $PM_{2.5}$ and a 5 % increase in PM_{10} surface concentrations. Due to drawback in mapping of dust particles with radii between 0.1 and 0.46 µm from GOCART to MOSAIC bins for Mie calculations of aerosol optical properties, the modeled AOD was decreased by 25 %–30 % in comparison with the corrected WRF-Chem version. This led to higher dust emissions and surface PM concentrations, because the WRF-Chem model is tuned to fit the simulated AOD to AERONET observations. This explains the inconsistencies found in Kumar et al. (2014), Eltahan et al. (2018), and Flaounas et al. (2017). Flaounas et al. (2017) noted that the model simulates realistic AODs when dust emissions are exaggerated, which in turn results in exaggerated dust surface concentrations. Conversely, realistic reproduction of dust concentration yields AODs that are smaller than in observations. Because of the error in calculating gravitational settling, dust column loadings increased by 4 %–6 % and the mass of gravitationally settled dust increased by 5 %–10 % in comparison with the corrected WRF-Chem version. The contribution of dust and sea salt into PM_{10} surface concentration was also higher by 2 %–4 % on average over the ME.

The cumulative effect of all inconsistencies was estimated in the 7-month case study conducted for 1 June–31 December 2016, when both AERONET AODs and PM_{10} surface

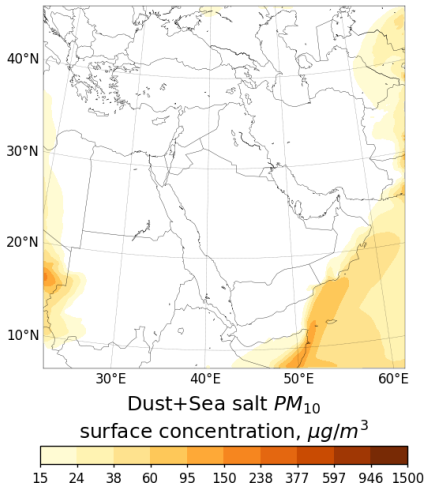

Figure 10. Effect of transboundary transport. Averaged dust and sea salt PM_{10} surface concentrations ($\mu g\,m^{-3}$) are obtained from the WRF-Chem simulation without emission of sea salt and dust.

observations were available. The comparison of runs with and without proposed changes shows that the run without corrections yields higher dust loadings and total dust mass in the atmosphere by 80 % and 60 %, respectively. This 7-month case study shows that the cumulative response to all code modifications applied simultaneously is stronger than the sum of their partial contributions. For instance, AOD underestimation causes higher dust emissions, which causes higher dust surface concentrations and increased production of dust in the atmosphere due to the error in gravitational settling. As a consequence, PM_{10} surface concentration further increases. Finally, an already high PM_{10} surface concentration becomes even higher due to the incorrect calculation of PM_{10}. Thus, the proposed improvements help to explain the considerable bias towards higher PM_{10} concentrations found in Ma et al. (2019), Flaounas et al. (2017), Su and Fung (2015), Nabavi et al. (2017), Rizza et al. (2017), and Eltahan et al. (2018).

In the course of improving the simulation of natural and anthropogenic aerosols and chemicals, we developed the capability to use MERRA-2 reanalysis for constructing WRF-Chem initial and boundary conditions for chemical species and aerosols. The interpolation utility Merra2BC was coded for this purpose. Boundary conditions constructed using MERRA-2 reanalysis more realistically account for the transboundary transport of aerosols. Merra2BC is made available to the community.

We believe the detailed quantification of the effects of the recent WRF-Chem code improvements are in line with open-source principles. The results of this work aim at better understanding of the model sensitivities to physical parameterizations. This work will add a greater understanding of model performance and will be especially helpful for those who use the WRF-Chem model coupled with the GOCART aerosol module to carry out dust simulations over regions where dust plays an important role.

Appendix A: Merra2BC interpolator

The Merra2BC interpolator (Ukhov and Stenchikov, 2020) (available online at https://github.com/saneku/Merra2BC) creates initial and boundary conditions based on MERRA-2 reanalysis (Randles et al., 2017) for a WRF-Chem simulation by interpolating chemical species mixing ratios defined on the MERRA-2 grid to WRF-Chem grid. For the initial conditions, interpolated values are written to each node of the WRF-Chem grid. For the boundary conditions, only boundary nodes are affected.

Merra2BC is written in Python. The utility requires additional modules that need to be installed in the Python environment: NetCDF4 (netcdf4, https://github.com/Unidata/netcdf4-python, last access: 20 January 2021) interface to work with NetCDF files and SciPy's (scipy, https://github.com/scipy/scipy, last access: 20 January 2021) interpolation package.

The full MERRA-2 reanalysis data set including aerosol and gaseous collections is publicly available online (https://disc.gsfc.nasa.gov/daac-bin/FTPSubset2.pl, last access: 20 January 2021). Depending on the requirements, all or one of the following aerosol and gaseous collections need to be downloaded: *inst3_3d_aer_Nv* – gaseous and aerosol mass mixing ratios, ($\mathrm{kg\,kg^{-1}}$) and *inst3_3d_chm_Nv* – carbon monoxide and ozone mass mixing ratios, ($\mathrm{kg\,kg^{-1}}$). Besides downloaded mass mixing ratios, pressure thickness *DELP* and surface pressure *PS* fields also need to be downloaded. Spatial coverage of the MERRA-2 files should include the area of the simulation domain. The time span of the downloaded files should match the start and duration of the simulation. More information regarding MERRA-2 files' specification is provided in Bosilovich et al. (2016).

A1 Reconstruction of the pressure in MERRA-2 and in WRF-Chem

Atmospheric pressure is used as a vertical coordinate. Latitude and longitude serve as the horizontal coordinates.

The MERRA-2 vertical grid has 72 model layers which are on a terrain-following hybrid $\sigma - p$ coordinate. The pressure at the model top is a fixed constant, $P_{\mathrm{TOP}} = 0.01$ hPa. Pressure at the model edges is computed by summing the *DELP* starting at P_{TOP}. A representative pressure for the layer can then be obtained by averaging pressure values on adjacent edges. Indexing for the vertical coordinate is from top to bottom; i.e., the first layer is the top layer of the atmosphere (P_{TOP}), while the 72nd layer is adjacent to the Earth's surface.

In WRF-Chem, the pressure field is not given in *wrfinput_d01* and *wrfbdy_d01* files. Hence, the pressure field must be restored using surface pressure P_{SFC} taken from *met_em_...** files created by *metgrid.exe* during the preprocessing stage. Pressure at the top of the model *wrf_p_top* and η values on half levels (*znu*) are taken from the *wrfinput_d01* file. The procedure of reconstructing the pressure from *met_em_...** files using the Python code is demonstrated in Fig. A1.

```
def get_pressure_from_metfile(metfile):
      PSFC=metfile.variables['PSFC'][:]
      WRF_Pres = np.zeros([nz,ny,nx])
      for z_level in reversed(range(nz)):
            WRF_Pres[nz-1-z_level,:]=PSFC*znu[0,z_level] +
                        (1.0 - znu[0,z_level])*wrf_p_top
      return WRF_Pres
```

Figure A1. A Python script, which reconstructs the pressure using the *met_em_...** files. nx, ny, and nz indicate the number of grid nodes in WRF-Chem domain.

A2 Mapping chemical species between MERRA-2 and WRF-Chem

Merra2BC file *config.py* contains multiplication factors to convert MERRA-2 mass mixing ratios of gases given in $\mathrm{kg\,kg^{-1}}$ into ppmv. Aerosols are converted from $\mathrm{kg\,kg^{-1}}$ to $\mathrm{\mu g\,kg^{-1}}$. When using the GOCART aerosol module in WRF-Chem simulation, all MERRA-2 aerosols and gases are matched with those from WRF-Chem. We simply multiply by a factor of 10^9 to convert MERRA-2 aerosol mixing ratios given in $\mathrm{kg\,kg^{-1}}$ into $\mathrm{\mu g\,kg^{-1}}$. In the case of gases, we need to multiply MERRA-2 mass mixing ratios by a ratio of molar masses $M_{\mathrm{air}}/M_{\mathrm{gas}}$ multiplied by 10^6 to convert $\mathrm{kg\,kg^{-1}}$ into ppmv, where M_{gas} and M_{air} are molar masses ($\mathrm{g\,mol^{-1}}$) of the required gas and air ($28.97\ \mathrm{g\,mol^{-1}}$), respectively. If another aerosol module is chosen in WRF-Chem, then different multiplication factors should be used.

A3 Interpolation procedure

A brief description of the interpolation procedure applied to the initial conditions is presented in Fig. A2.

For boundary conditions, the procedure is similar, except that additional updates of domain boundary tendencies are required and interpolation is performed for each step, where boundary conditions are applied.

A4 Typical workflow

Here are the steps describing how to work with the Merra2BC interpolator:

1. Run *real.exe*, which will produce initial *wrfinput_d01* and boundary conditions *wrfbdy_d01* files required by the WRF-Chem simulation.
2. Download required MERRA-2 files from https://disc.gsfc.nasa.gov/daac-bin/FTPSubset2.pl;
3. Download Merra2BC from https://github.com/saneku/Merra2BC.

Algorithm 1 Interpolation procedure applied to initial conditions

1: Pressure reconstruction at each node of the MERRA-2 and WRF-Chem grids.

2: **for** each 72 vertical layers in MERRA-2 grid **do**

3: Horizontal interpolation of MERRA-2 pressure on WRF-Chem latitude, longitude nodes using bivariate spline approximation (method *RectBivariateSpline* from Scipy module).

4: **Result**: MERRA-2 pressure is calculated on 72 levels but on latitude, longitude nodes of the WRF-Chem grid.

5: **for** each chemical species mixing ratio **do**

6: **for** each 72 vertical layers in MERRA-2 grid **do**

7: Horizontal interpolation of MERRA-2 species mixing ratio on WRF-Chem latitude, longitude nodes using bivariate spline approximation (method *RectBivariateSpline* from Scipy module).

8: **Result**: MERRA-2 species mixing ratio is calculated on 72 levels but on latitude, longitude nodes of WRF-Chem grid.

9: **for** each lat, long node of the WRF-Chem grid **do**

10: Vertical linear interpolation of MERRA-2 species mixing ratio on WRF-Chem vertical coordinate (method *interp1d* from from Scipy module).

11: **Result**: MERRA-2 species mixing ratio is interpolated at each node of WRF-Chem grid.

12: Multiplying interpolated species mixing ratio by corresponding factor to convert kg/kg into ppmv or ug/kg, depending whether it gas or aerosol.

13: Updating corresponding fields in WRF-Chem *wrfinput_d01* file by interpolated values.

14: **Result**: WRF-Chem grid is updated by interpolated values from MERRA-2 grid.

Figure A2. Interpolation procedure applied to initial conditions.

4. Edit the *config.py* file which contains

   a. mapping of chemical species and aerosols between MERRA-2 and WRF-Chem;

   b. paths to *wrfinput_d01*, *wrfbdy_d01*, and *met_em_...** files;

   c. a path to the downloaded MERRA-2 files.

5. *real.exe* sets default boundary and initial conditions for some chemical species. Merra2BC adds interpolated values to the existing values, which may cause incorrect concentration values. To avoid this, run "python *zero_fileds.py*", which will zero the required fields.

6. Run "python *main.py*", which will do the interpolation. As a result, files *wrfinput_d01* and *wrfbdy_d01* will be updated by the interpolated from MERRA-2 values.

7. Modify the WRF-Chem *namelist.input* file at section *&chem*: set *have_bcs_chem = .true.* to activate updated boundary conditions and, if needed, *chem_in_opt = 1* to activate updated initial conditions.

8. Run *wrf.exe*.

Appendix B: Statistics

The following statistical parameters were used to quantify the level of agreement between estimations and observations.

For the Pearson correlation coefficient (R),

$$R = \frac{\sum_{i=1}^{N}\left(F_i - \overline{F}\right)\left(O_i - \overline{O}\right)}{\sqrt{\sum_{i=1}^{N}\left(F_i - \overline{F}\right)^2 \sum_{i=1}^{N}\left(O_i - \overline{O}\right)^2}}. \tag{B1}$$

For the mean bias (*bias*),

$$\text{bias} = \frac{1}{N}\sum_{i=1}^{N}\left(F_i - O_i\right), \tag{B2}$$

where F_i is the estimated value, O_i is the observed value, $\overline{F} = \frac{1}{N}\sum_{i=1}^{N} F_i$ and $\overline{O} = \frac{1}{N}\sum_{i=1}^{N} O_i$ their averages, and N is the number of data.

Appendix C: AOD calculations

WRF-Chem does not calculate AOD at 550 nm (only at 300, 400, 600, and 1000 nm for variables *TAUAER1*, *TAUAER2*, *TAUAER3*, and *TAUAER4*, respectively), but instead it outputs the extinction coefficient at 550 nm (variable *EXTCOF55*). The AOD at 550 nm (AOD_{550}) for the (i, j) vertical column can be calculated by summing throughout the vertical column of product of multiplication of the *EXTCOF55* by the Δz:

$$\text{AOD}_{550 i,j} = \sum_{k}\text{EXTCOF55}_{i,j,k} \cdot \Delta z_{i,j,k}, \tag{C1}$$

where $\Delta z_{i,j,k}$ is the depth (m) of the (i, j, k) cell, which can be computed using the formula:

$$\Delta z_{i,j,k} = \left(\text{PH}_{i,j,k} + \text{PHB}_{i,j,k}\right)/g - \left(\text{PH}_{i,j,k-1} + \text{PHB}_{i,j,k-1}\right)/g, \tag{C2}$$

where PH is the geopotential and PHB is the perturbed geopotential, and $g = 9.81\,\text{m s}^2$ is the gravitational acceleration. Variables PH and PHB are taken from the WRF-Chem output.

To facilitate comparison with the model output, the 550 nm AOD is calculated using the following relation:

$$\frac{\tau_\lambda}{\tau_{\lambda_0}} = \left(\frac{\lambda}{\lambda_0}\right)^{-\alpha}, \tag{C3}$$

where α is the Ångström exponent for the 440–675 nm wavelength range provided by AERONET, τ_λ is the optical thickness at wavelength λ, and τ_{λ_0} is the optical thickness at the reference wavelength λ_0.

Appendix D: Column loadings

WRF-Chem stores dust column loadings ($\mu g\,m^{-2}$) using variables *DUSTLOAD_1,2,3,4,5*. Column loadings for the (i, j) vertical column of other aerosols or chemical species can be computed by vertically summing throughout the vertical column of product of multiplication of the mass mixing ratio q ($\mu g\,kg^{-1}$) by the cell depth Δz (m) (see Eq. C2) and dry air density ($kg\,m^{-3}$). WRF outputs variable *ALT*, which is inverse dry air density ($m^3\,kg^{-1}$):

$$\text{Column loading}_{i,j} = \sum_k q_{i,j,k} \cdot \Delta z_{i,j,k} \cdot 1/\text{ALT}_{i,j,k}. \quad \text{(D1)}$$

WRF-Chem outputs gases concentrations expressed in ppmv. Conversion from ppmv to the mass mixing ratio can be calculated using the following formula:

$$\text{Mass mixing ratio} = \text{ppmv} \cdot 10^{-6} \cdot M_{\text{gas}}/M_{\text{air}}, \quad \text{(D2)}$$

where M_{gas} and M_{air} are molar masses ($g\,mol^{-1}$) of the required gas and air ($28.97\,g\,mol^{-1}$), respectively.

Appendix E: Surface concentrations

Surface concentration ($\mu g\,m^{-3}$) of an aerosol at (i, j) vertical column can be computed by multiplication of the mass mixing ratio ($\mu g\,kg^{-1}$) at the first model level (q_1) by the corresponding dry air density ($kg\,m^{-3}$) at the first model level ($1/\text{ALT}_1$):

$$\text{Surface concentration}_{i,j} = q_{i,j,1} \cdot 1/\text{ALT}_{i,j,1}. \quad \text{(E1)}$$

To obtain gas surface concentration ($\mu g\,m^{-3}$), ppmv needs to be converted to the mass mixing ratio; see Eq. (D2).

Appendix F: Dust mass balance

In WRF-Chem's GOCART aerosol module, dust emissions along with three types of removal processes (dry deposition, gravitational settling, and wet scavenging) are implemented. Here, for the sake of clarity, we refrain from consideration of wet scavenging. To calculate the dust mass balance, assuming there is no flow of dust through the domain boundaries, we need to calculate the amount of dust emitted from the domain area, the amount of dust that was deposited by gravitational settling and dry deposition, and the amount of dust in the atmosphere. By default, WRF-Chem stores instantaneous values of dust emission and deposition fluxes. We modified the WRF-Chem code to accumulate the dust emission and deposition fluxes.

F1 Grid column area

In WRF, one of the following four projections can be used: the Lambert conformal, polar stereographic, Mercator, and latitude–longitude projections. These projections are implemented using map factors. In the computational space, the grid lengths Δx (m) and Δy (m) (dx and dy variables in *namelist.input*) in x and y directions are constants. In the physical space, distances between grid points vary with position on the grid. Map factors $mx_{i,j}$ and $my_{i,j}$ for both the x and y components are used for the transformation from computational to physical space and computed by *geogrid.exe* during the preprocessing stage. $mx_{i,j}$ and $my_{i,j}$ are defined as the ratio of the distance in computational space to the corresponding distance on the Earth's surface (Skamarock et al., 2008):

$$\left(mx_{i,j}, my_{i,j}\right) = (\Delta x, \Delta y)/\left(\text{distance on the Earth}_{i,j}\right). \quad \text{(F1)}$$

Map factors $mx_{i,j}$ and $my_{i,j}$ for each (i, j) vertical column are stored in *wrfinput_d01* file in variables *MAPFAC_MX* and *MAPFAC_MY*, respectively. Thus, the area of (i, j) column $S_{i,j}$ (m^2) in physical space is calculated using the following formula:

$$S_{i,j} = \left(\Delta x/mx_{i,j}\right) \cdot \left(\Delta y/my_{i,j}\right). \quad \text{(F2)}$$

F2 Dust emission

For demonstration purposes, we use the original GOCART-WRF dust emission scheme (*dust_opt*=1) implemented in subroutine *gocart_dust_driver()* file *module_gocart_dust.F*. In this scheme, instantaneous dust emission flux ($kg\,s^{-1}$ cell), calculated for each dust, bin is stored in the variables *EDUST1,2,3,4,5*. Other dust emission schemes (*dust_opt*=2,3) store instantaneous dust emission flux expressed in $g\,m^{-2}\,s^{-1}$ and $\mu g\,m^{-2}\,s^{-1}$, respectively. Thus, multiplying this flux by Δt on each time step and by adding the value obtained to the previous value, we accumulate dust emission (kilograms per cell) from each surface grid cell. Thus, emission of dust from the first dust bin *Emitted dust*$_1$ (kg) is calculated using the following formula:

$$\text{Emitted dust}_1 = \sum_{i,j} \left(S_{i,j}/\Delta x \cdot \Delta y\right) \cdot \text{EDUST1}_{i,j}, \quad \text{(F3)}$$

where $S_{i,j}$ is the area of the (i, j) column (m^2); see Eq. (F2). Here, we divide $S_{i,j}$ by $\Delta x \cdot \Delta y$ to account for the fact that in the subroutine *gocart_dust_driver()* dust emission are calculated in the computational space where grid cells have dimensions Δx and Δy.

F3 Gravitational settling and dry deposition

The subroutines *settling()* implemented in *module_gocart_settling.F* and *gocart_drydep_driver()* implemented in *module_gocart_drydep.F* are used to calculate gravitational settling and dry deposition of dust. By default, instantaneous gravitational and dry deposition fluxes ($\mu g\,m^{-2}\,s^{-1}$) are stored in variables *GRASET_1,2,3,4,5* and *DRYDEP_1,2,3,4,5*, respectively. Thus, multiplying these

fluxes on each time step by the time step Δt and the scaling coefficient 10^{-9}, and by adding the resulting value to the previous value, we obtain accumulated gravitational and dry deposition mass per unit area expressed in (kg m^{-2}).

Hence, deposition of the dust from the first dust bin due to gravitational settling (*Grav. settled dust*$_1$, kg) and dry deposition (*Dry deposited dust*$_1$, kg) is calculated using the following formulas:

$$\text{Grav. settled dust}_1 = \sum_{i,j} S_{i,j} \cdot \text{GRASET\_1}_{i,j}, \tag{F4}$$

$$\text{Dry deposited dust}_1 = \sum_{i,j} S_{i,j} \cdot \text{DRYDEP\_1}_{i,j}, \tag{F5}$$

where $S_{i,j}$ is the area of the (i, j) column (m^2); see Eq. (F2).

F4 Dust in the atmosphere

There are two approaches to calculate the amount of dust in the atmosphere (*Dust in the atmosphere*, kg). In the first approach, we use dust column loadings (variables *DUSTLOAD_1,2,3,4,5*, µg m^{-2}). Thus, the mass of dust in the first dust bin is given:

$$\text{Dust in the atmosphere}_1 = 10^{-9} \cdot \sum_{i,j} S_{i,j} \cdot \text{DUSTLOAD\_1}_{i,j}, \tag{F6}$$

where $S_{i,j}$ is the area of the (i, j) column (m^2); see Eq. (F2).

In the second approach, we calculate the mass of air in each grid cell, multiply it by the dust mass mixing ratio (for example, DUST$_1$, µg kg^{-1}) and sum over all grid cells in the domain:

$$\text{Dust in the atmosphere}_1 = 10^{-9} \cdot \sum_{i,j} S_{i,j} \cdot \sum_{k} \text{DUST}_{1i,j,k} \cdot \Delta z_{i,j,k} \cdot 1/\text{ALT}_{i,j,k}, \tag{F7}$$

where $\Delta z_{i,j,k}$ is the depth (m) (see Eq. C2) and $\text{ALT}_{i,j,k}$ is the inverse dry air density (m^3 kg^{-1}) in the grid cell (i, j, k).

Gaseous concentrations expressed in ppmv need to be converted into mass mixing ratios (µg kg^{-1}); see Eq. (D2).

Code and data availability. The standard version of WRF-Chem is publicly available online at https://github.com/wrf-model/WRF (Skamarock et al., 2008). The Merra2BC interpolator is available online at https://doi.org/10.5281/zenodo.3695911 (Ukhov and Stenchikov, 2020).

Author contributions. AU planned and performed the calculations, wrote the manuscript, and led the discussion. RA, GG, and GS participated in the discussion and reviewed the manuscript.

Competing interests. The authors declare that they have no conflict of interest.

Acknowledgements. In this work, we used AERONET data from the KAUST Campus site that was maintained by Illia Shevchenko with the help of the NASA Goddard Space Flight Center AERONET team. We thank Brent Holben and Alexander Smirnov for the monitoring and regular calibrations of our instruments. We also used data from the Sede Boker and Mezaira sites and would like to thank their principal investigators (Arnon Karnieli and Brent Holben).

For computer time, this research used the resources of the Supercomputing Laboratory at KAUST.

The authors also would like to thank the three anonymous reviewers for their helpful comments.

Financial support. This research has been supported by the King Abdullah University of Science and Technology (KAUST, grant no. URF/1/2180-01-01).

Review statement. This paper was edited by Samuel Remy and reviewed by three anonymous referees.

References

Alghamdi, M. A., Almazroui, M., Shamy, M., Redal, M. A., Alkhalaf, A. K., Hussein, M. A., and Khoder, M. I.: Characterization and elemental composition of atmospheric aerosol loads during springtime dust storm in western Saudi Arabia, Aerosol Air Qual. Res., 15, 440–453, 2015.

Anisimov, A., Tao, W., Stenchikov, G., Kalenderski, S., Prakash, P. J., Yang, Z.-L., and Shi, M.: Quantifying local-scale dust emission from the Arabian Red Sea coastal plain, Atmos. Chem. Phys., 17, 993–1015, https://doi.org/10.5194/acp-17-993-2017, 2017.

Bagnold, R.: The physics of blown sand and desert dunes, William Morrow & Company N.D., New York, USA, 1941.

Bangalath, H. K. and Stenchikov, G.: Role of dust direct radiative effect on the tropical rain belt over Middle East and North Africa: A high-resolution AGCM study, J. Geophys. Res.-Atmos., 120, 4564–4584, https://doi.org/10.1002/2015JD023122, 2015.

Banks, J. R., Brindley, H. E., Stenchikov, G., and Schepanski, K.: Satellite retrievals of dust aerosol over the Red Sea and the Persian Gulf (2005–2015), Atmos. Chem. Phys., 17, 3987–4003, https://doi.org/10.5194/acp-17-3987-2017, 2017.

Barnard, J. C., Fast, J. D., Paredes-Miranda, G., Arnott, W. P., and Laskin, A.: Technical Note: Evaluation of the WRF-Chem "Aerosol Chemical to Aerosol Optical Properties" Module using data from the MILAGRO campaign, Atmos. Chem. Phys., 10, 7325–7340, https://doi.org/10.5194/acp-10-7325-2010, 2010.

Belly, P.: Sand movement by wind, Tech. Mem. 1, US Army Coastal Eng. Res. Cent., Washington, D.C., USA, 1964.

Bian, H., Tie, X., Cao, J., Ying, Z., Han, S., and Xue, Y.: Analysis of a severe dust storm event over China: application of the WRF-dust model, Aerosol Air Qual. Res., 11, 419–428, 2011.

Bosilovich, M., Lucchesi, R., and Suarez, M.: MERRA-2: File specification GMAO Office Note No. 9 (Version 1.1), available at: https://gmao.gsfc.nasa.gov/pubs/docs/Bosilovich785.pdf (last access: 20 January 2021), 2016.

Bukowski, J. and van den Heever, S. C.: Convective distribution of dust over the Arabian Peninsula: the impact of model resolution, Atmos. Chem. Phys., 20, 2967–2986, https://doi.org/10.5194/acp-20-2967-2020, 2020.

Chen, S., Zhao, C., Qian, Y., Leung, L. R., Huang, J., Huang, Z., Bi, J., Zhang, W., Shi, J., Yang, L., Li, D., and Li, J.: Regional modeling of dust mass balance and radiative forcing over East Asia using WRF-Chem, Aeolian Res., 15, 15–30, 2014.

Chen, S., Yuan, T., Zhang, X., Zhang, G., Feng, T., Zhao, D., Zang, Z., Liao, S., Ma, X., Jiang, N., Zhang, J., Yang, F., and Lu, H.: Dust modeling over East Asia during the summer of 2010 using the WRF-Chem model, J. Quant. Spectrosc. Ra., 213, 1–12, 2018.

Chin, M., Ginoux, P., Kinne, S., Torres, O., Holben, B. N., Duncan, B. N., Martin, R. V., Logan, J. A., Higurashi, A., and Nakajima, T.: Tropospheric aerosol optical thickness from the GOCART model and comparisons with satellite and Sun photometer measurements, J. Atmos. Sci., 59, 461–483, 2002.

Dee, D. P., Uppala, S., Simmons, A., Berrisford, P., Poli, P., Kobayashi, S., Andrae, U., Balmaseda, M., Balsamo, G., Bauer, D. P., Bechtold, P., Beljaars, A. C. M., Van de Berg, L., Bidlot, J., Bormann, N., Delsol, C., Dragani, R., Fuentes, M., Geer, A. J., Haimberger, L., Healy, S. B., Hersbach, H., Hólm, E. V., Isaksen, L., Kållberg, P., Köhler, M., Matricardi, M., McNally, A. P., Monge-Sanz, B. M., Morcrette, J.-J., Park, B.-K., Peubey, C., de Rosnay, P., Tavolato, C., Thépaut, J.-N., and Vitart, F.: The ERA-Interim reanalysis: Configuration and performance of the data assimilation system, Q. J. Roy. Meteor. Soc., 137, 553–597, 2011.

Dipu, S., Prabha, T. V., Pandithurai, G., Dudhia, J., Pfister, G., Rajesh, K., and Goswami, B.: Impact of elevated aerosol layer on the cloud macrophysical properties prior to monsoon onset, Atmos. Environ., 70, 454–467, 2013.

Dubovik, O. and King, M. D.: A flexible inversion algorithm for retrieval of aerosol optical properties from Sun and sky radiance measurements, J. Geophys. Res.-Atmos., 105, 20673–20696, 2000.

Eltahan, M., Shokr, M., and Sherif, A. O.: Simulation of severe dust events over Egypt using tuned dust schemes in weather research forecast (WRF-Chem), Atmosphere, 9, 246, https://doi.org/10.3390/atmos9070246, 2018.

Emmons, L. K., Walters, S., Hess, P. G., Lamarque, J.-F., Pfister, G. G., Fillmore, D., Granier, C., Guenther, A., Kinnison, D., Laepple, T., Orlando, J., Tie, X., Tyndall, G., Wiedinmyer, C., Baughcum, S. L., and Kloster, S.: Description and evaluation of the Model for Ozone and Related chemical Tracers, version 4 (MOZART-4), Geosci. Model Dev., 3, 43–67, https://doi.org/10.5194/gmd-3-43-2010, 2010.

Farahat, A.: Air pollution in the Arabian Peninsula (Saudi Arabia, the United Arab Emirates, Kuwait, Qatar, Bahrain, and Oman): causes, effects, and aerosol categorization, Arab. J. Geosci., 9, 196, https://doi.org/10.1007/s12517-015-2203-y, 2016.

Fast, J., Gustafson Jr, W., Easter, R., Zaveri, R., Barnard, J., Chapman, E., Grell, G., and Peckham, S.: Evolution of ozone, particulates, and aerosol direct forcing in an urban area using a new fully-coupled meteorology, chemistry, and aerosol model, J. Geophys. Res, 111, D21305, https://doi.org/10.1029/2005JD006721, 2006.

Fast, J., Aiken, A. C., Allan, J., Alexander, L., Campos, T., Canagaratna, M. R., Chapman, E., DeCarlo, P. F., de Foy, B., Gaffney, J., de Gouw, J., Doran, J. C., Emmons, L., Hodzic, A., Herndon, S. C., Huey, G., Jayne, J. T., Jimenez, J. L., Kleinman, L., Kuster, W., Marley, N., Russell, L., Ochoa, C., Onasch, T. B., Pekour, M., Song, C., Ulbrich, I. M., Warneke, C., Welsh-Bon, D., Wiedinmyer, C., Worsnop, D. R., Yu, X.-Y., and Zaveri, R.: Evaluating simulated primary anthropogenic and biomass burning organic aerosols during MILAGRO: implications for assessing treatments of secondary organic aerosols, Atmos. Chem. Phys., 9, 6191–6215, https://doi.org/10.5194/acp-9-6191-2009, 2009.

Flaounas, E., Kotroni, V., Lagouvardos, K., Klose, M., Flamant, C., and Giannaros, T. M.: Assessing atmospheric dust modelling performance of WRF-Chem over the semi-arid and arid regions around the Mediterranean, Atmos. Chem. Phys. Discuss. [preprint], https://doi.org/10.5194/acp-2016-307, 2016.

Flaounas, E., Kotroni, V., Lagouvardos, K., Klose, M., Flamant, C., and Giannaros, T. M.: Sensitivity of the WRF-Chem (V3.6.1) model to different dust emission parametrisation: assessment in the broader Mediterranean region, Geosci. Model Dev., 10, 2925–2945, https://doi.org/10.5194/gmd-10-2925-2017, 2017.

Forster, P., Ramaswamy, V., Artaxo, P., Berntsen, T., Betts, R., Fahey, D., Haywood, J., Lean, J., Lowe, D., Myhre, G., Nganga, J., Prinn, R., Raga, G., Schulz, M., and Van Dorland, R.: Climate change 2007: the physical science basis, Contribution of Working Group I to the Fourth Assessment Report of the Intergovernmental Panel on Climate Change, Cambridge University Press, Cambridge, UK and New York, NY, USA, p. 212, 2007.

Fountoukis, C., Ackermann, L., Ayoub, M. A., Gladich, I., Hoehn, R. D., and Skillern, A.: Impact of atmospheric dust emission schemes on dust production and concentration over the Arabian Peninsula, Modeling Earth Systems and Environment, 2, 115, https://doi.org/10.1007/s40808-016-0181-z, 2016.

Ghan, S. J. and Zaveri, R. A.: Parameterization of optical properties for hydrated internally mixed aerosol, J. Geophys. Res.-Atmos., 112, D10201, https://doi.org/10.1029/2006JD007927, 2007.

Gillette, D. A. and Passi, R.: Modeling dust emission caused by wind erosion, J. Geophys. Res.-Atmos., 93, 14233–14242, 1988.

Ginoux, P., Chin, M., Tegen, I., Prospero, J. M., Holben, B., Dubovik, O., and Lin, S.-J.: Sources and distributions of dust aerosols simulated with the GOCART model, J. Geophys. Res.-Atmos., 106, 20255–20273, 2001.

Gong, S.: A parameterization of sea-salt aerosol source function for sub- and super-micron particles, Global Biogeochem. Cy., 17, 1097, https://doi.org/10.1029/2003GB002079, 2003.

Grell, G. A., Peckham, S. E., Schmitz, R., McKeen, S. A., Frost, G., Skamarock, W. C., and Eder, B.: Fully coupled "online" chemistry within the WRF model, Atmos. Environ., 39, 6957–6975, 2005.

Holben, B. N., Eck, T. F., Slutsker, I., Tanre, D., Buis, J., Setzer, A., Vermote, E., Reagan, J., Kaufman, Y., Nakajima, T., Lavenu, F., Jankowiak, I., and Smirnov, A.: AERONET – A federated instrument network and data archive for aerosol characterization, Remote Sens. Environ., 66, 1–16, 1998.

Huang, Q., Marsham, J. H., Parker, D. J., Tian, W., and Grams, C. M.: Simulations of the effects of surface heat flux anomalies on stratification, convective growth, and vertical transport within the Saharan boundary layer, J. Geophys. Res.-Atmos., 115, D05201, https://doi.org/10.1029/2009JD012689, 2010.

Jish Prakash, P., Stenchikov, G., Kalenderski, S., Osipov, S., and Bangalath, H.: The impact of dust storms on the Arabian Peninsula and the Red Sea, Atmos. Chem. Phys., 15, 199–222, https://doi.org/10.5194/acp-15-199-2015, 2015.

Kalenderski, S. and Stenchikov, G.: High-resolution regional modeling of summertime transport and impact of African dust over the Red Sea and Arabian Peninsula, J. Geophys. Res.-Atmos., 121, 6435–6458, 2016.

Kalenderski, S., Stenchikov, G., and Zhao, C.: Modeling a typical winter-time dust event over the Arabian Peninsula and the Red Sea, Atmos. Chem. Phys., 13, 1999–2014, https://doi.org/10.5194/acp-13-1999-2013, 2013.

Karagulian, F., Temimi, M., Ghebreyesus, D., Weston, M., Kondapalli, N. K., Valappil, V. K., Aldababesh, A., Lyapustin, A., Chaouch, N., Al Hammadi, F., and Abdooli, A.: Analysis of a severe dust storm and its impact on air quality conditions using WRF-Chem modeling, satellite imagery, and ground observations, Air Qual. Atmos. Hlth., 12, 1–18, 2019.

Khan, B., Stenchikov, G., Weinzierl, B., Kalenderski, S., and Osipov, S.: Dust plume formation in the free troposphere and aerosol size distribution during the Saharan Mineral Dust Experiment in North Africa, Tellus B, 67, 27170, https://doi.org/10.3402/tellusb.v67.27170, 2015.

Kumar, R., Barth, M. C., Pfister, G. G., Naja, M., and Brasseur, G. P.: WRF-Chem simulations of a typical pre-monsoon dust storm in northern India: influences on aerosol optical properties and radiation budget, Atmos. Chem. Phys., 14, 2431–2446, https://doi.org/10.5194/acp-14-2431-2014, 2014.

LeGrand, S. L., Polashenski, C., Letcher, T. W., Creighton, G. A., Peckham, S. E., and Cetola, J. D.: The AFWA dust emission scheme for the GOCART aerosol model in WRF-Chem v3.8.1, Geosci. Model Dev., 12, 131–166, https://doi.org/10.5194/gmd-12-131-2019, 2019.

Lihavainen, H., Alghamdi, M., Hyvärinen, A.-P., Hussein, T., Aaltonen, V., Abdelmaksoud, A., Al-Jeelani, H., Almazroui, M., Almehmadi, F., Al Zawad, F., Hakala, J., Khoder, M., Neitola, K., Petäjä, T., Shabbaj, I. I., and Hämeric, K.: Aerosols physical properties at Hada Al Sham, western Saudi Arabia, Atmos. Environ., 135, 109–117, 2016.

Liu, S., McKeen, S., Hsie, E.-Y., Lin, X., Kelly, K., Bradshaw, J., Sandholm, S., Browell, E., Gregory, G., Sachse, G., Bandy, A., Thornton, D., Blake, D., Rowland, F., Newell, R., Heikes, B.,

Singh, H., and Talbot, R.: Model study of tropospheric trace species distributions during PEM-West A, J. Geophys. Res.-Atmos., 101, 2073–2085, 1996.

Ma, S., Zhang, X., Gao, C., Tong, D. Q., Xiu, A., Wu, G., Cao, X., Huang, L., Zhao, H., Zhang, S., Ibarra-Espinosa, S., Wang, X., Li, X., and Dan, M.: Multimodel simulations of a springtime dust storm over northeastern China: implications of an evaluation of four commonly used air quality models (CMAQ v5.2.1, CAMx v6.50, CHIMERE v2017r4, and WRF-Chem v3.9.1), Geosci. Model Dev., 12, 4603–4625, https://doi.org/10.5194/gmd-12-4603-2019, 2019.

Marticorena, B. and Bergametti, G.: Modeling the atmospheric dust cycle: 1. Design of a soil-derived dust emission scheme, J. Geophys. Res.-Atmos., 100, 16415–16430, 1995.

Miller, R. and Tegen, I.: Climate response to soil dust aerosols, J. Climate, 11, 3247–3267, 1998.

Nabavi, S. O., Haimberger, L., and Samimi, C.: Sensitivity of WRF-chem predictions to dust source function specification in West Asia, Aeolian Res., 24, 115–131, 2017.

Nguyen, H. D., Riley, M., Leys, J., and Salter, D.: Dust storm event of February 2019 in Central and East Coast of Australia and evidence of long-range transport to New Zealand and Antarctica, Atmosphere, 10, 653, https://doi.org/10.3390/atmos10110653, 2019.

O'Neill, N., Eck, T., Smirnov, A., Holben, B., and Thulasiraman, S.: Spectral discrimination of coarse and fine mode optical depth, J. Geophys. Res.-Atmos., 108, 4559, https://doi.org/10.1029/2002JD002975, 2003.

Osipov, S. and Stenchikov, G.: Simulating the regional impact of dust on the Middle East climate and the Red Sea, J. Geophys. Res.-Oceans, 123, 1032–1047, 2018.

Osipov, S., Stenchikov, G., Brindley, H., and Banks, J.: Diurnal cycle of the dust instantaneous direct radiative forcing over the Arabian Peninsula, Atmos. Chem. Phys., 15, 9537–9553, https://doi.org/10.5194/acp-15-9537-2015, 2015.

Parajuli, S. P., Stenchikov, G. L., Ukhov, A., and Kim, H.: Dust emission modeling using a new high-resolution dust source function in WRF-Chem with implications for air quality, J. Geophys. Res.-Atmos., 124, 10109–10133, 2019.

Parajuli, S. P., Stenchikov, G. L., Ukhov, A., Shevchenko, I., Dubovik, O., and Lopatin, A.: Aerosol vertical distribution and interactions with land/sea breezes over the eastern coast of the Red Sea from lidar data and high-resolution WRF-Chem simulations, Atmos. Chem. Phys., 20, 16089–16116, https://doi.org/10.5194/acp-20-16089-2020, 2020.

Powers, J. G., Klemp, J. B., Skamarock, W. C., Davis, C. A., Dudhia, J., Gill, D. O., Coen, J. L., Gochis, D. J., Ahmadov, R., Peckham, S. E., Grell, G. A., Michalakes, J., Trahan, S., Benjamin, S. G., Alexander, C. R., Dimego, G. J., Wang, W., Schwartz, C. S., Romine, G. S., Liu, Z., Snyder, C., Chen, F., Barlage, M. J., Yu, W., and Duda, M. G.: The weather research and forecasting model: Overview, system efforts, and future directions, B. Am. Meteorol. Soc., 98, 1717–1737, 2017.

Randles, C., da Silva, A. M., Buchard, V., Colarco, P., Darmenov, A., Govindaraju, R., Smirnov, A., Holben, B., Ferrare, R., Hair, J., et al.: The MERRA-2 aerosol reanalysis, 1980 onward. Part I: System description and data assimilation evaluation, J. Climate, 30, 6823–6850, 2017.

Rizza, U., Barnaba, F., Miglietta, M. M., Mangia, C., Di Liberto, L., Dionisi, D., Costabile, F., Grasso, F., and Gobbi, G. P.: WRF-Chem model simulations of a dust outbreak over the central Mediterranean and comparison with multi-sensor desert dust observations, Atmos. Chem. Phys., 17, 93–115, https://doi.org/10.5194/acp-17-93-2017, 2017.

Rizza, U., Miglietta, M. M., Mangia, C., Ielpo, P., Morichetti, M., Iachini, C., Virgili, S., and Passerini, G.: Sensitivity of WRF-Chem model to land surface schemes: Assessment in a severe dust outbreak episode in the Central Mediterranean (Apulia Region), Atmos. Res., 201, 168–180, 2018.

Shao, Y.: A model for mineral dust emission, J. Geophys. Res.-Atmos., 106, 20239–20254, 2001.

Shao, Y.: Simplification of a dust emission scheme and comparison with data, J. Geophys. Res.-Atmos., 109, D10202, https://doi.org/10.1029/2003JD004372, 2004.

Shao, Y., Ishizuka, M., Mikami, M., and Leys, J.: Parameterization of size-resolved dust emission and validation with measurements, J. Geophys. Res.-Atmos., 116, D08203, https://doi.org/10.1029/2010JD014527, 2011.

Skamarock, W. C., Klemp, J. B., Dudhia, J., Gill, D. O., Barker, D. M., Wang, W., and Powers, J. G.: A description of the advanced research WRF version 2, Tech. rep., National Center For Atmospheric Research Boulder Co Mesoscale and Microscale Meteorology Div, Boulder, CO, USA, 2005.

Skamarock, W. C., Klemp, J. B., Dudhia, J., Gill, D. O., Barker, D., Duda, M., Huang, X. Y., Wang, W., and Powers, J. G.: A description of the Advanced Research (WRF) model, Version 3, Natl. Ctr. Atmos. Res., Boulder, CO, USA, available at: https://github.com/wrf-model/WRF (last access: 20 January 2021), 2008.

Su, L. and Fung, J. C.: Sensitivities of WRF-Chem to dust emission schemes and land surface properties in simulating dust cycles during springtime over East Asia, J. Geophys. Res.-Atmos., 120, 11–215, 2015.

Sulaiman, S. A., Singh, A. K., Mokhtar, M. M. M., and Bou-Rabee, M. A.: Influence of Dirt Accumulation on Performance of PV Panels, Energ. Proc., 50, 50–56, https://doi.org/10.1016/j.egypro.2014.06.006, 2014.

Ukhov, A. and Stenchikov, G.: Merra2BC. Interpolation utility for boundary and initial conditions used in WRF-Chem, Zenodo, https://doi.org/10.5281/zenodo.3695911, 2020.

Ukhov, A., Mostamandi, S., da Silva, A., Flemming, J., Alshehri, Y., Shevchenko, I., and Stenchikov, G.: Assessment of natural and anthropogenic aerosol air pollution in the Middle East using MERRA-2, CAMS data assimilation products, and high-resolution WRF-Chem model simulations, Atmos. Chem. Phys., 20, 9281–9310, https://doi.org/10.5194/acp-20-9281-2020, 2020a.

Ukhov, A., Mostamandi, S., Krotkov, N., Flemming, J., da Silva, A., Li, C., Fioletov, V., McLinden, C., Anisimov, A., Alshehri, Y. M., and Stenchikov, G.: Study of SO Pollution in the Middle East Using MERRA-2, CAMS Data Assimilation Products, and High-Resolution WRF-Chem Simulations, J. Geophys. Res.-Atmos., 125, e2019JD031993, https://doi.org/10.1029/2019JD031993, 2020b.

Wang, K., Zhang, Y., Yahya, K., Wu, S.-Y., and Grell, G.: Implementation and initial application of new chemistry-aerosol options in WRF/Chem for simulating secondary organic aerosols

and aerosol indirect effects for regional air quality, Atmos. Environ., 115, 716–732, 2015.

Watson, A. J., Bakker, D., Ridgwell, A., Boyd, P., and Law, C.: Effect of iron supply on Southern Ocean CO_2 uptake and implications for glacial atmospheric CO_2, Nature, 407, 730–733, https://doi.org/10.1038/35037561, 2000.

Yuan, T., Chen, S., Huang, J., Zhang, X., Luo, Y., Ma, X., and Zhang, G.: Sensitivity of simulating a dust storm over Central Asia to different dust schemes using the WRF-Chem model, Atmos. Environ., 207, 16–29, 2019.

Zaveri, R. A., Easter, R. C., Fast, J. D., and Peters, L. K.: Model for simulating aerosol interactions and chemistry (MOSAIC), J. Geophys. Res.-Atmos., 113, D13204, https://doi.org/10.1029/2007JD008782, 2008.

Zhang, Y., Liu, Y., Kucera, P. A., Alharbi, B. H., Pan, L., and Ghulam, A.: Dust modeling over Saudi Arabia using WRF-Chem: March 2009 severe dust case, Atmos. Environ., 119, 118–130, 2015.

Zhao, C., Liu, X., Leung, L. R., Johnson, B., McFarlane, S. A., Gustafson Jr., W. I., Fast, J. D., and Easter, R.: The spatial distribution of mineral dust and its shortwave radiative forcing over North Africa: modeling sensitivities to dust emissions and aerosol size treatments, Atmos. Chem. Phys., 10, 8821–8838, https://doi.org/10.5194/acp-10-8821-2010, 2010.

Zhao, C., Liu, X., Ruby Leung, L., and Hagos, S.: Radiative impact of mineral dust on monsoon precipitation variability over West Africa, Atmos. Chem. Phys., 11, 1879–1893, https://doi.org/10.5194/acp-11-1879-2011, 2011.

Zhao, C., Liu, X., and Leung, L. R.: Impact of the Desert dust on the summer monsoon system over Southwestern North America, Atmos. Chem. Phys., 12, 3717–3731, https://doi.org/10.5194/acp-12-3717-2012, 2012.

Zhao, C., Chen, S., Leung, L. R., Qian, Y., Kok, J. F., Zaveri, R. A., and Huang, J.: Uncertainty in modeling dust mass balance and radiative forcing from size parameterization, Atmos. Chem. Phys., 13, 10733–10753, https://doi.org/10.5194/acp-13-10733-2013, 2013.

Zhu, X., Prospero, J., and Millero, F. J.: Diel variability of soluble Fe (II) and soluble total Fe in North African dust in the trade winds at Barbados, J. Geophys. Res.-Atmos., 102, 21297–21305, 1997.